NTNU
Norwegian University of
Science and Technology

Laboratory Testing to Study Initiation and Evolution of Shale Barriers

Lars Erik Austbø

Preface

This master thesis is written as a part of the MSc. programme in Petroleum Technology for the Department of Petroleum Engineering and Applied Geophysics at the Norwegian University of Science and Technology (NTNU) in Trondheim, Norway. The experiments were conducted at a SINTEF laboratory.

I want to extent my gratitude to my supervisor professor Rune M. Holt for his theoretical guidance during the last year of my studies, and Jørn Stenebråten for helping me in the laboratory.

I also want to thank my fellow students and friends for five fantastic years in Trondheim, and my family for support.

Lars Erik Austbø

Trondheim, June 2016

Abstract

Clay and shale formations occur naturally with sealing properties, and are therefore investigated as possible annular barriers. The properties of these argillaceous rocks are not fully understood with regards to creep of clay and shale. The aim of this thesis was to do experiments on a Pierre shale in order to observe if creep at elevated temperatures could attribute to create a natural annular barrier.

The study mainly focused on the dilation process of argillaceous rocks and thermal effects. The clay-stones are highly dependent of their hydraulic conductivity, permeability, failure strength, swelling properties, thermal expansion etc. Two tests were conducted to assess the sealing properties of a Pierre shale.

An attempt was made to find out how thermal effects and water content affected the clay behaviour, and in which magnitude. The thermo-hydro-mechanical behaviour of the clays proved to be important since it affects the rock during its lifespan, and it was observed that the pore water plays a central role in the deformation process of clays.

Sammendrag

Skifere har naturlige gode egenskaper som er gunstige for å hindre strømning av væsker på grunn av deres lave permeabilitet, og er dermed vurdert som en tett annulær barriere. Skifersoner med passende egenskaper blir brukt som en annulær barriere i stedet for sement. Hvis det viser seg at den utvalgte skifersonen har de rette egenskapene som skal til for å danne og opprettholde barrieren, er det mye tid og penger som kan bli spart. På bakgrunn av dette har det blitt gjennomført en studie av hvordan skifere og leirer blir påvirket av økende trykk og temperaturer over tid. Det har blitt lagt spesielt vekt på hvordan den aksielle deformasjonen endrer seg ved økende temperaturer og hvordan permeabiliteten blir påvirket.

To forsøk på kjerneprøver fra en Pierre-skifer ble gjennomført i en ødometercelle. Kjerneprøvene ble utsatt for en enaksiell last opptil 30 kN, og temperaturer opptil 100˚C for observere hvordan det påvirket den aksielle deformasjonsraten og permeabiliteten. Målet med forsøkene var å observere hva som påvirket de egenskapene som skifersonene må ha for å danne og opprettholde en annulær barriere.

Table of Contents

List of Figures

List of Tables

Nomenclature

T	Absolute temperature
cP	Centipoise
F_{corr}	Correction factor
A	Cross-sectional area of the core sample
$°C$	Degrees Celsius

K	Degrees Kelvin
ρ	Density
d	Diameter of the core sample
μ	Dynamic viscosity
K_m	Experimental setup constant
α	Exponential decline factor
F	Force
g	Gravity
h	Height of core sample
L	Length of core sample
α_V	Linear thermal expansion coefficient
m	Mass
F_{mech}	Mechanical loading frame factor
N	Newton
k	Permeability
ϑ	Poisson's ratio
r	Radius
R_0	Resistance
ε	Strain
σ	Stress
a	Value for dynamic viscosity

b	Value for dynamic viscosity
c	Value for dynamic viscosity
β	Volume expansion coefficient
S	Weight fraction of NaCl
E	Young's mudulus

Abbrevations

XLOT	Extended leak off test
GF	Gauge factor
LVDT	Linear variable differential transformer
NORSOK	Norsk sokkels konkurranseposisjon
NaCl	Sodium Chloride
THM	Thermo-hydro-mechanical
USB	Universal serial bus

1 Introduction

The ability of shale to form sealing barriers around oil and gas wells has been documented in the literature, in particular with experience from Statoil's work in the North Sea (Williams, 2009). The use of the formation instead of cement, in particular for plug and abandonment, may lead to extremely large cost savings, and possibly also in better barriers. In order to make this a robust technology, there is a need to understand the mechanisms that lead to formation of barriers, and if and how these may be triggered and stimulated.

Time dependent deformation through creep is thought to be a key mechanism in establishment of a shale barrier. Creep is the deformation of a material under constant stress conditions. Notice that it may be difficult to distinguish creep from consolidation (pore pressure equilibration) in laboratory tests, in particular if the pore pressure is not reliably measured.

SINTEF is performing a Joint Industry Project with additional support from The Norwegian Research Council, with the main objectives being to understand how and under what conditions such barriers are formed, and to identify possible ways of enhancing the barrier forming capability. As part of this, experimental work was performed, simulating the formation of shale barriers under controlled stress and temperature conditions with small samples in the laboratory.

The purpose of this thesis was to look into theory and experiments regarding clay and shale as a sealing formation for very long periods of time. Thus, time dependent deformation and thermal effects have been addressed in this thesis. Experiments were conducted on a Pierre shale and the result was supposed to be representative for what is aimed for in order to seal petroleum wells.

2 Background

Borehole stability during drilling is a challenge, and one of the factors that might ruin the favourable conditions is creep. If a rock surpasses its yield point it might creep to failure and lead to borehole collapse. The creep behaviour is usually considered as a problem since it complicates casing running and drilling. However, it can be used as a benefit in order to create a secondary annular barrier outside of the casing.

Using the formation as a secondary barrier is applicable in several situations, for instance as a plug and abandonment strategy or before side tracking. Since many countries demand two independent barriers in order to mitigate the risk of leakage from the reservoir to the surface, this technique is very relevant given proper geological circumstances and properties. There are several advantages by using the formation as a secondary barrier. Firstly, it is cost saving since it is a natural process and excludes the use of cement. Secondly, it creates a safer and better barrier than an artificial one.

The use of cement as a secondary barrier requires a lot of attention with respect to calculations of the correct composition and setting time, in addition to the required storage capacity. The cementing operations are expensive, time consuming and damaging the casing. Thus, low permeable formations such as shales are considered as a better alternative as a secondary barrier given proper circumstances. Borehole logging is often used as a method for checking the surrounding formations and are able to identify which low permeable zones that can completely seal off the gap between the casing and the formation, in order to create a natural annular barrier. If the log response is not reliable, pressure testing of the sealed off zones is an alternative option. Using the formation as a secondary barrier has proven to be successful in over 40 wells in the North Sea (Williams, 2009). The criteria for success relies on the properties and extent of the low permeable zones. The zones must have a sufficient length parallel to the well trajectory and consist in a uniform matter around the casing if the formation is going to provide the required safety. Even though it might seem like a formation is suitable for being a barrier, it is not given due to the physical properties of the rock.

2.1 Shale and Clay Formations

Naturally occurring argillaceous rocks are considered as impermeable sealing cap rocks due to their sealing properties. Some of these properties are mechanical strength, permeability, homogeneity, swelling potential and a visco-plastic behaviour (Klinkenberg, 2008). Argillaceous rocks are commonly found in the crust of the earth and are known for their sealing abilities which might prevent fluids from migrating towards the biosphere. The argillaceous rocks decreases in permeability with increasing depth.

Argillaceous rocks are formed after many millions of years with compaction and sedimentation, which impacts their mechanical properties. The compaction history of argillaceous rocks affects their mechanical and thermal properties which determines their overconsolidation ratio, while the sedimentation process determines the homogeneity and internal structure of the argillaceous sediments (Blümling, 2006). Heterogeneities in the matrix tend to decrease the maximum strength of the rock due to earlier fracture initiation.

Clay mainly consist of fine grained minerals which alters its properties if the clay is exposed to heat, pressure or saturation effects (Klinkenberg, 2008). The minerals are classified by their shape, grain size and composition. The most common minerals are kaolinite with a mixture of chlorite, illite, smectite (swelling mineral) and other layered minerals (Klinkenberg, 2008). The mineral composition affects the anisotropic and mechanical behaviour of the clay. It is difficult to characterize clays from a mechanical point of view due to their ductile matrix, high porosity and dilating minerals. Many experiments have been conducted on argillaceous rocks to determine their mechanical behaviour, where the following observations were made. A Callovo-Oxfordian argillite became more brittle and stiffer with increasing calcite content, and more ductile with increasing clay content (Chiarelli, 2000). Cataclastic and granular creep behaviour was observed in a long-term test of a Callovo-Oxfordian argillite. Cracks originated from the large pyrite grains in the clay matrix, and not from the small carbonate or quartz grains (Fabre, 2006). A mixture of pyrite, carbonates and quartz weakens the matrix structure which are lowering the threshold for fracture initiation (Fouche, 2004). Thus, it is difficult to predict the mechanical behaviour of the clay.

Stress redistribution might cause consolidation and swelling of the argillaceous rock. Suction pressure might attract water to the lower pressurized zones where stress has been reduced, resulting in swelling of the clay particles. Increasing water content leads to a decrease of the undrained shear

strength and the deformation modulus (Corkum, 2005). The total porosity and the distance between the clay particles which affects the attractive and repulsive particle forces of a rock can be determined by the water content of a fully saturated rock. Since the total porosity of the rock varies with time due to swelling and compression, it affects the rock strength. Argillaceous rocks are sensitive to water since it affects their mechanical behaviour.

Estimating correct formation properties is challenging since the most accurate data is collected by taking core samples which are supposed to represent large sections of the formation. Even though precautions are taken during core sample retrieval, the core samples slightly alter their physical properties when they are extracted from their in-situ conditions. Possible changes of the extracted core samples are volume, saturation, pore pressure, applied stress, mechanical cracking and temperature. These alterations makes it even harder to retrieve accurate data, in order to get a good estimate of the rock mass behaviour. The rock mass behaviour can be determined by using two different methods, the short-term or the long-term behaviour method. The long-term behaviour method requires sufficient numerical modelling to simulate the rock mass processes, while the short-term behaviour method requires tests on-site after the first wells are drilled.

2.1.1 Sealing Properties

The stress redistributes in the formation after it is drilled through, this might cause fracture initiation around the borehole where the stresses have been altered. If argillaceous rocks are supposed to be an annular barrier, it is important that these fractures are sealed. Heating of the clay makes it more ductile, this might lead to sealing of the fracture. Self-sealing decreases the hydraulic conductivity and reduces the permeability of the clay.

The sealing properties of a soft Boom clay were tested by fracturing a sample and measure the hydraulic conductivity as the clay sample self-sealed. The clay exhibited a rapid sealing response after it was fractured and saturated, which is usual for soft clays due to their lower strength. (Blümling, 2006). Figure 2.1 depicts two images of the clay, where the first image shows the clay after it was fractured and the other image shows the clay after the sealing process.
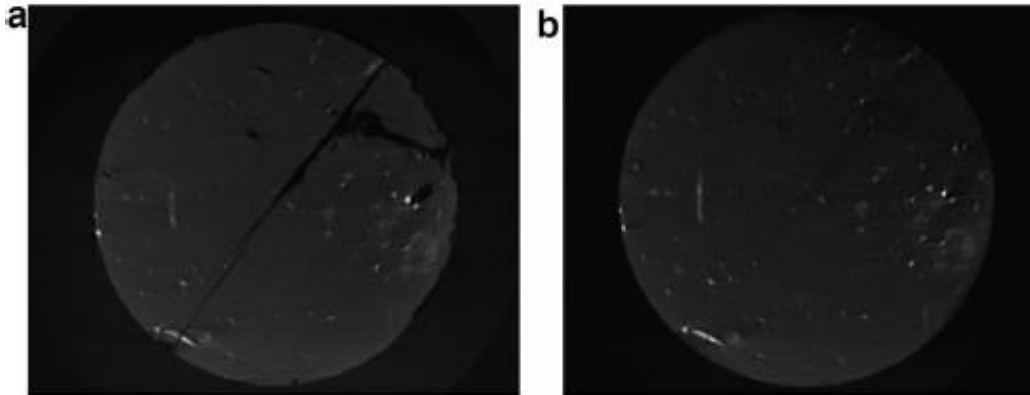
Figure 2.1: Boom Clay sample (Blümling, 2006)

The hydraulic conductivity of the clay nearly reached its original value after the sealing process, which indicates good self-sealing abilities. There are several processes which might have caused the permeability decrease of the clay, it could have been swelling, disintegration of the sample, shear compaction, creep or chemical reactions.

2.2 Shale as a Barrier

A permanent annular barrier must contain the following properties; non-shrinking, impermeable, ductile, long term integrity, wetting and resistance to different substances (NORSOK). None of these requirements states which substance the barrier should be, only its properties. Thus, shale can be elected since it fulfils all of the criteria. Shale is known for its abilities as a sealing cap rock and it is therefore logical that it may suit in being a secondary barrier as well. A more specific approach to the NORSOK standards states that the rock has to be an impermeable shale, where gamma ray logs, electrical logs and cuttings description logs are helpful tools in the determination process. The rock strength has to withstand the maximum pressure in the reservoir. The area which the shale has to cover along the well trajectory must be sufficient, and the formation displacement mechanisms must fulfil the requirements in order to maintain a functioning annular barrier. All of these specific requirements will be discussed further.

The formation displacement mechanisms is the first subject that will be discussed. These mechanisms are displacing the formation towards the wellbore, resulting in a borehole radius reduction. Shear failure and creep are considered as the most important causes, while chemical effects, consolidation, compaction failure, tensile failure and thermal expansion are of less importance (Fjær, 2008). The formation displacement is considered to be initiated when the drilling

5

fluid pressure becomes lower than the pore pressure of the formation. This allows the formation to creep in a hydraulic way towards the wellbore. Consolidation and compaction failure might occur after the formation has expanded because of the stress redistribution. This could cause a rapid shock for the formation and close the annulus if fractures were absent during the failure process.

The next subject that will be discussed is the formation strength. The minimal horizontal stress of the formation must be higher than the maximum reservoir pressure if the barrier is supposed to be sufficient. A strength test of the barrier can be applied to check if the calculated stress model correlates with the measured formation strength, and to ensure the absence of any fluid communication systems in the barrier. An extended leak off test (XLOT) is an example of a test that measures the formation strength by pressurizing the annulus.

If the pressure testing of a tight shale section has proven that it is suitable for being a barrier, the associated bond log may be used as a template in the determination of future annular barriers without pressure testing. A single bond log response from a specific formation is a rough method for determining barriers in adjacent formations due to different properties, therefore the bond log response should be updated by taking new pressure tests when entering new formations. Annular barriers were determined using bond logs during plug and abandonment operations on the Norwegian Continental Shelf in 2007 and 2008 with a 90% success rate (Williams, 2009).

The casing setting is important to ensure stability of the borehole due to the stress redistributions which occurs after a borehole is drilled. After the casing is set, a proper natural annular barrier might be created within a few weeks if the creep rate is rapid and the distance from the casing to the formation is relatively small. By using shale as an annular barrier has not only led to an improved wellbore integrity, but also reduced the time and costs. In addition to being self-healing and more solid than the human made barriers (Williams, 2009).

2.2.1 Field Experience
A Shetland clay formation was considered as a secondary annular barrier in a plug and abandonment strategy, therefore logging tools were run confirm if the formation was adequate. The results from these tests are depicted in Figure 2.2. The grey arrows in this figure depicts the sections where the clay has dilated and compacted onto the casing, while the red arrows represents three

Shetland chalk sections which appears as liquid filled pockets. The key observation in this example is the liquid filled pockets since they lack small rock particles. Rock fragments is typical for shear or tensile failure, which means that the formation must have behaved in a hydraulic way towards the casing. This observation supports the plastic creep theory.

An XLOT from a section in the Shetland formation is depicted in Figure 2.3. Area one in the figure indicates a much lower reservoir pressure compared to the annular pressure, which means that it is a hydraulic barrier present that isolates the reservoir from the annulus. Area two and three confirmed that the formation strength was sufficient to withstand the applied pressure.

Based on these results and the NORSOK standards, this Shetland clay formation may be applied as a secondary annular barrier and benefit future operations.
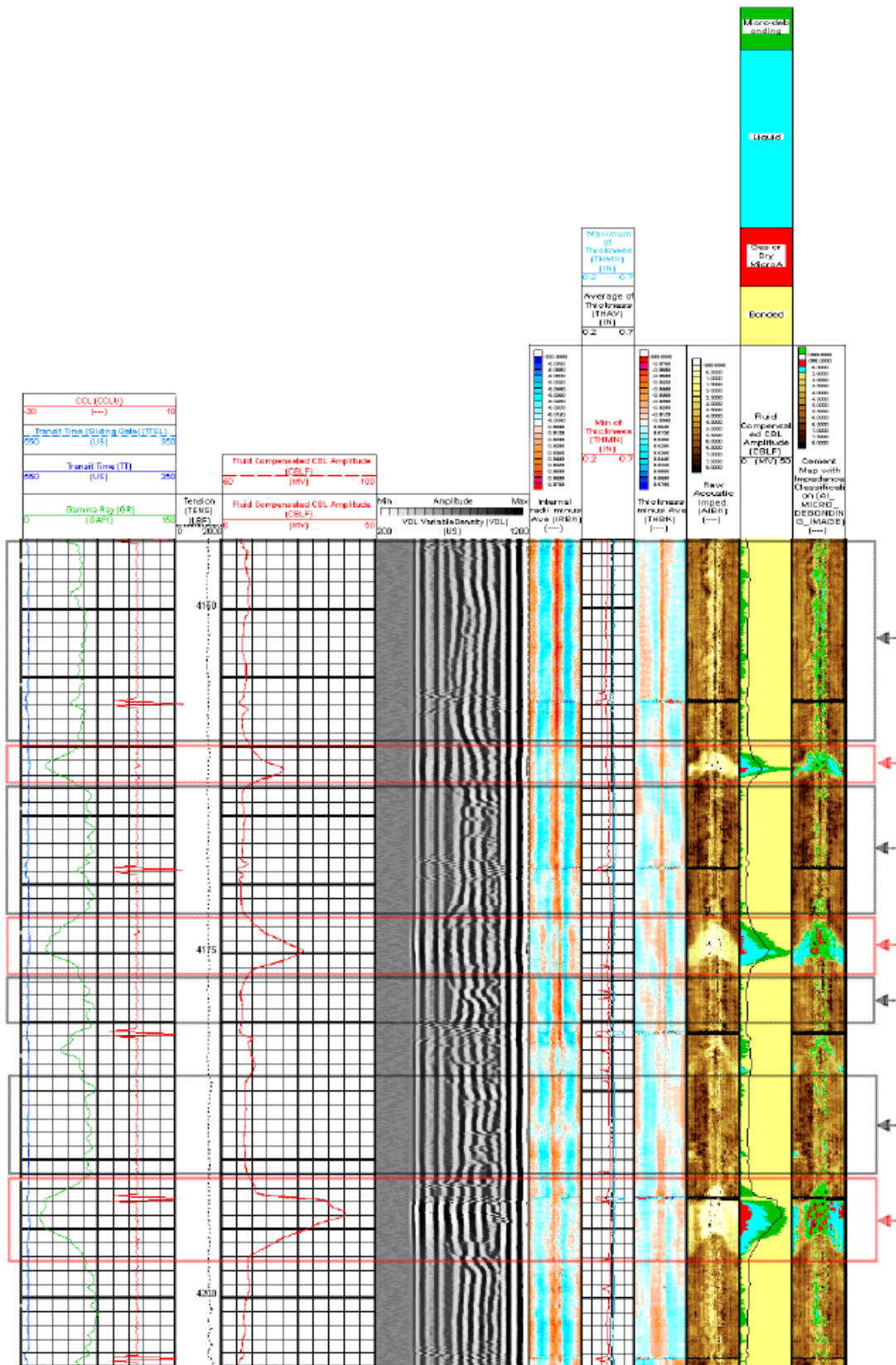
Figure 2.2: Logs over an interval in a Shetland clay formation (Williams, 2009).
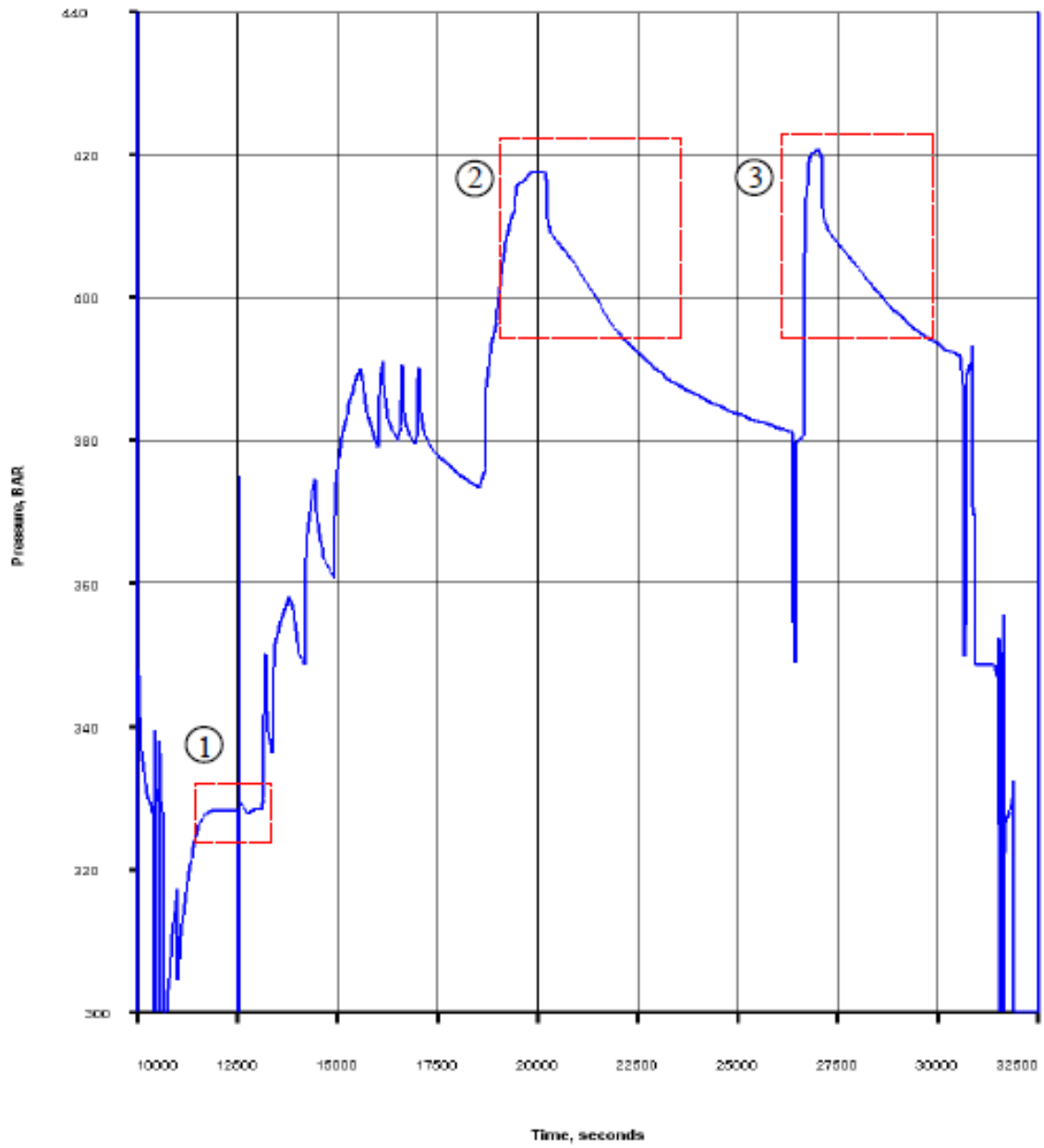
Figure 2.3: XLOT of a section in the Shetland Clay (Williams, 2009).

2.3 Creep

Creep is associated with a visco-elastic behaviour of the rock and might occur in both saturated and dry rocks. The creep behaviour is divided into three phases based on the rock's strain rate. The transient (primary) creep phase has a decreasing strain rate, the steady state (secondary) creep phase is recognizable by its constant strain rate, while the accelerating (tertiary) creep phase is characterized by its increasing strain rate, as depicted in Figure 2.4.
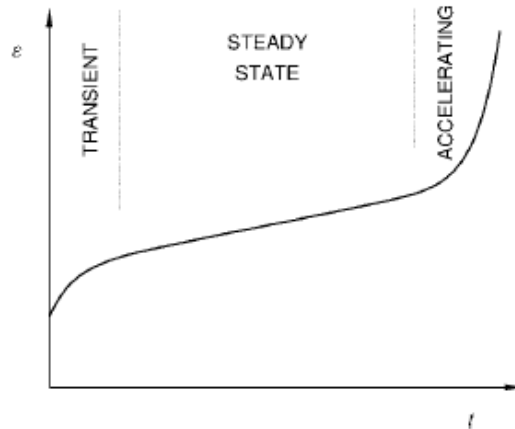
Figure 2.4: Time versus strain for a creeping rock (Fjær, 2008).

The creep behaviour varies with applied stress, as seen in Figure 2.5. A single creep phase might last from a couple of minutes to many years depending on the stress level. If a rock has been exposed to low stress for a long time, it might not reach the secondary creep phase due to a stabilization of the material, while a rock exposed to high stress might experience all the three creep phases during a short time period before it eventually fails.
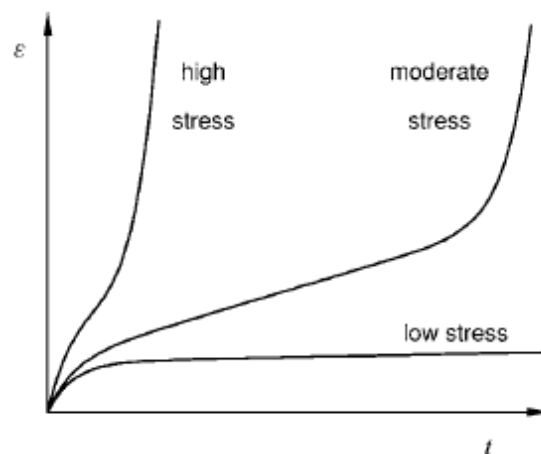
Figure 2.5: Creep development for different levels of applied stress (Fjær, 2008).

Several mathematical Equations and models like the Burgers model have been applied to characterize the creep behaviour, but these will not be focused on in this thesis. The creep rate tends to increase with temperature since creep is a molecular process which is affected by temperature (Fjær, 2008). Based on this statement the creep dependency of temperature is further investigated.

2.3.1 Creep in Argillaceous Rocks

The stresses in a formation redistributes after it is drilled through, this may cause large displacements around the borehole and lead to rock failure. Deformation of a rock under constant stresses is a typical creep mechanism and makes the formation act as a less viscous medium. This reduces the rock strength. The magnitude of the deformation is determined by the level of applied stress and available space for the formation to expand, it typically dilates towards lower pressurized areas such as the casing string. Argillaceous rocks have this trait which makes them suitable for creating natural barriers, other known traits are low permeability and good absorption capacity for radioactive ions (Fabre, 2006).

Creep tests were conducted on an Oxfordian argillite to identify the different creep phases, the secondary and tertiary creep phases were of interest since rock failure do not occur in the primary creep phase (Fabre, 2006). Multi-stage creep tests were performed on the Oxfordian argillite with increasing applied stress. Failure occurred in some of the core samples before they reached the tertiary creep phase, which means that the applied stress exceeded their long term rock strength. An observation from these tests was the axial viscoplastic strain which affected the total deformation of the core samples significantly, depicted in Figure 2.6. The core samples deformed at different times when they were under constant deviatoric stress, some deformed after a few weeks while others needed almost a year. Over 50% of the deformations were due to delayed strain.
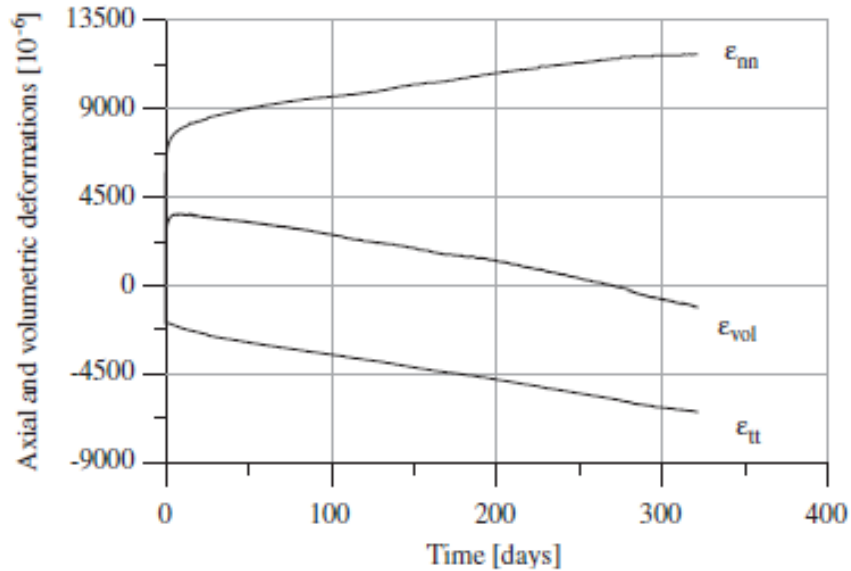
Figure 2.6: Oxfordian argillite under constant stress conditions (Fabre, 2006).

Argillaceous rocks have anisotropic properties which affects their deformation, failure and strength behaviour (Fabre, 2006). These properties originate from the way they were formed and the behaviour can be seen in Figure 2.6 where the argillite has compressed in the axial direction and dilated in the lateral direction. The total volume of the sample has decreased. This core sample only experienced the primary creep phase where it contracted, a dilation is not expected until it reaches the secondary creep phase. The core samples dilated and contracted differently during the three creep phases since each sample was unique with respect to its mineralogical properties. Other observations were the structural anisotropy and the amount of iron sulphides which affected the occurrence of a cracked matrix, and a viscosity dependency of cataclastic and granular creep. Cataclastic creep occurs when there is a delayed microstructural worsening of the rock, while granular creep occurs when the grains slide and rotates.

Another test was conducted to investigate the creep rate under constant confining stress, using a true triaxial compression test on an Opalinus clay. The primary creep phase was affected by the anisotropy of the core samples, as depicted in Figure 2.7.
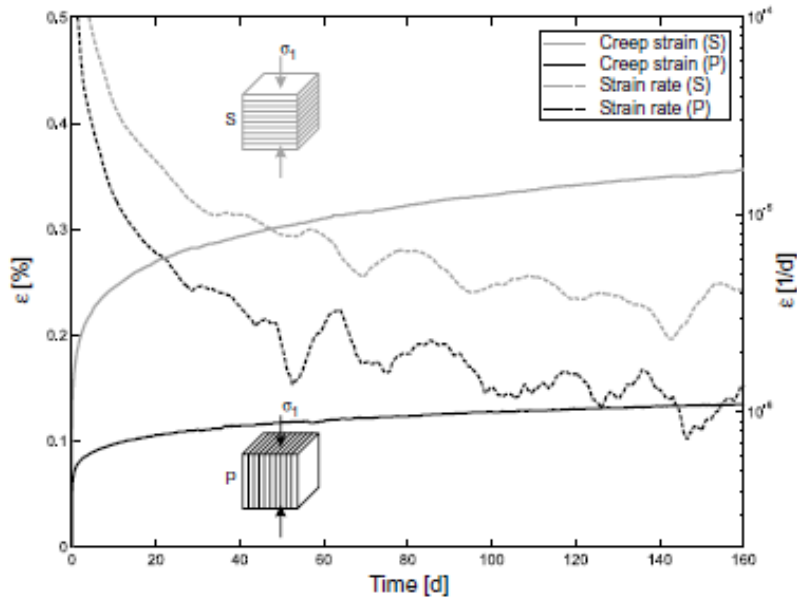
Figure 2.7: Deformation behaviourof samples loaded parallel (P) and normal (S) to the bedding plane (Neuman, 2005)

The core samples loaded normal to the bedding plane deformed more than the core samples loaded parallel to the bedding plane. During the first days of the test the deformation rates was different with respect to the core samples orientation, which indicates that the primary creep phase is highly affected by the anisotropy. After 200 days however, the deformation rates stabilized, which indicates that the secondary creep phase is not that affected of anisotropy (Neuman, 2005).

2.4 Thermal Effects

Clay particles which are susceptible for water usually swells due to the absorption of the water molecules. The pore space of a clay mainly consist of bound water under in-situ conditions, but with increasing temperature the energy within the water molecules increases as well and turns most of the bound water into free water. Many experiments have been conducted to address thermal effects and how it impacts argillaceous rocks, some of these experiments will be discussed further.

When a clay reaches a certain temperature a dilation process initiates due to an expansion of the molecules, and are later followed by a contraction period due to loss of water molecules at higher temperatures (Li, 2013). The contraction rate tends to increase with increasing temperature. This have a major impact on wellbores with high temperatures.

Figure 2.8 depicts a thermal experiment using triaxial tests on Kaolin clays with different overconsolidation ratios. The overconsolidated clays which have been exposed to the highest stresses and temperatures before dilated the most, while the normally consolidated clays contracted. The stress history of the clays affects the thermal volumetric strain based on the experimental results (Cekerevac, 2003).
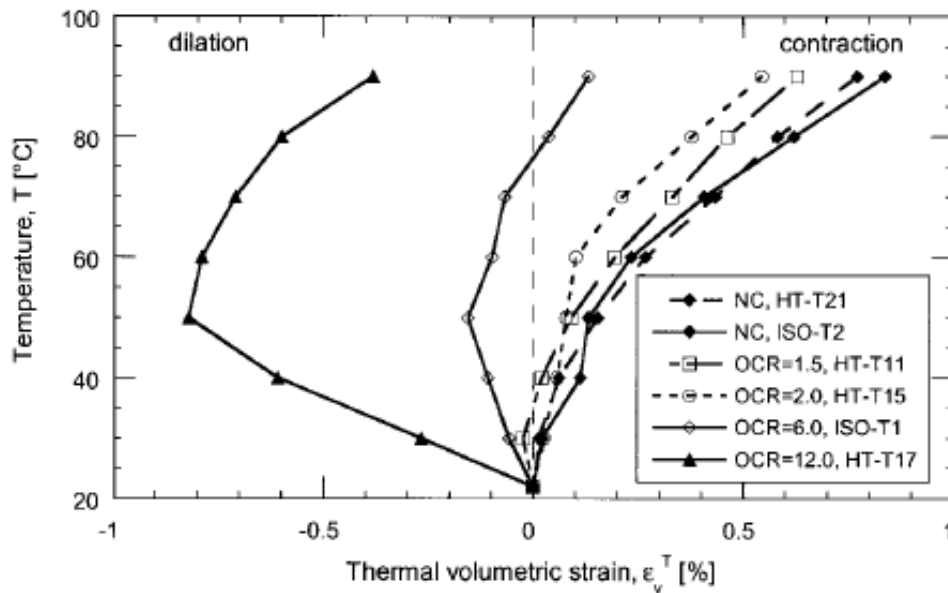
Figure 2.8: Thermal volumetric strain of a Kaolin clay during drained heating (Cekerevac, 2003)

2.4.1 Thermo-hydro-mechanical Behaviour of Indurated Clays

During the lifespan of an argillaceous rock, thermo-hydro-mechanical (THM) processes occurs. Thus, these processes are of importance since they are affecting the long term performance of a natural annular barrier. The water content of an indurated clay mainly consist of absorbed water at the mineral surface. These absorbed water particles are heavily bound to the clay surface and might not join the advective transport which is controlled by the hydrostatic pressure gradient (Horseman, 1996). However, a strong suction pressure might loosen the water particles from the clay surface and decrease the water content of the clay (Zhang, 2006). Therefore, the pore water is essential for the THM properties of indurated clays.

2.4.1.1 Experimental Results

Figure 2.9 depicts a thermal expansion test which was performed on an Opalinus clay from Mont Terri, where the following observations were made. Each temperature increase resulted in an expansion of the of the clay perpendicular to the bedding plane, this effect was not observed for the clay parallel to the bedding plane. During constant temperature, the clay contracted in both directions to the bedding plane due to loss of pore water. When the clay was cooled down there were a dilation in the parallel direction and a contraction in the perpendicular direction to the bedding plane. Since the thermal expansion coefficient for the clay oriented parallel to the bedding plane was an order of magnitude less than the clay oriented perpendicular to the bedding plane, the thermal behaviour of the Opalinus clay exhibit anisotropic properties.
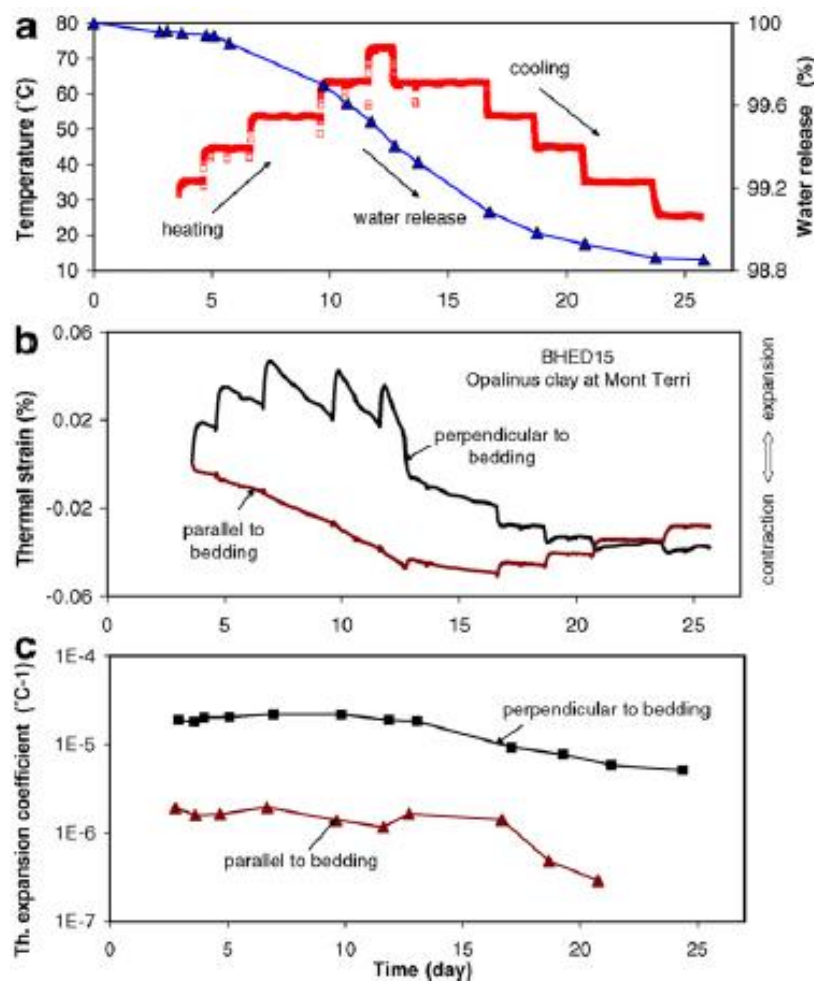
Figure 2.9: Thermal expansion test of Opalinus Clay (Zhang, 2006)

15

Figure 2.10 depicts uniaxial creep tests conducted on a Callovo-Oxfordian argillite, where the following observations were made. The creep behaviour occurred at a stress level lower than 1 MPa, which indicates the absence of a lower threshold for the creep initiation (Zhang, 2006). The three tests gave approximately the same signature response even though the core samples were exhibited to a different level of stress.
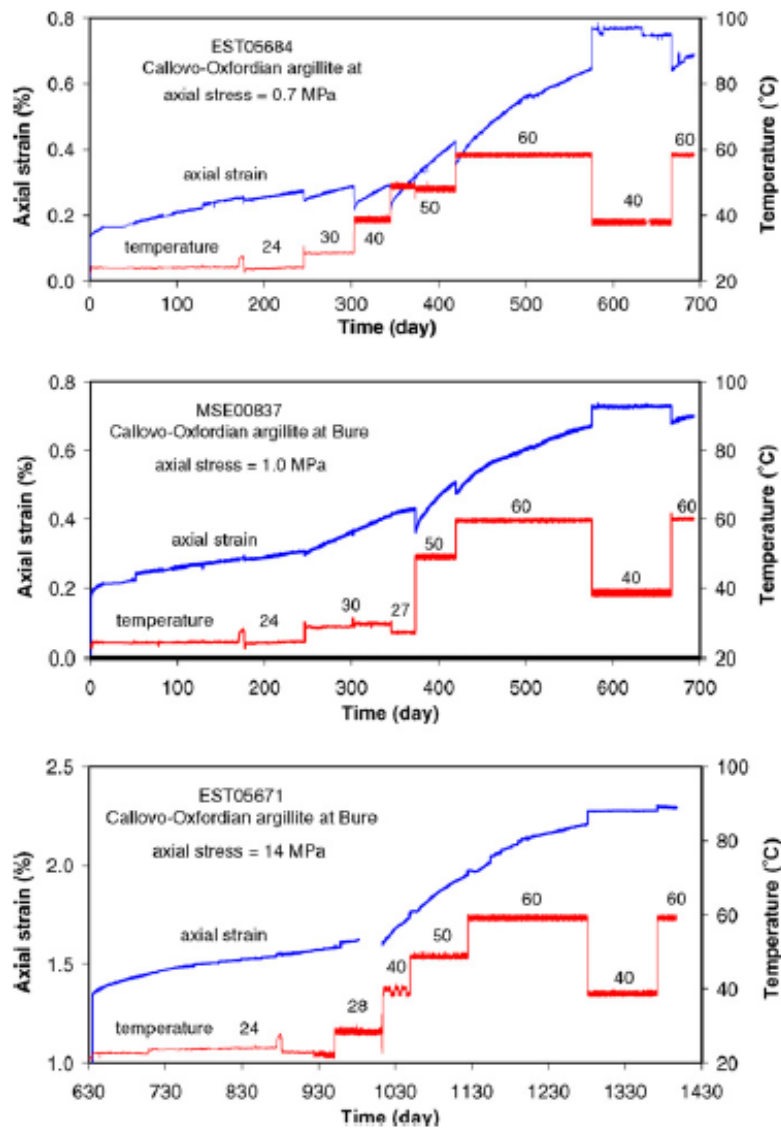
Figure 2.10: Creep behaviour of Callovo-Oxfordian argillite (Zhang, 2006)

A rapid increase in temperature led to a sudden drop of the axial strain, which implies an expansion of the argillite. This led to an increased creep rate of the argillite until the temperature reached approximately 50 degrees Celsius, as depicted in Figure 2.11. Loss of heated pore water might be

the cause for the creep rate decrease after the temperature exceeded 50 degrees Celsius. A relationship between the creep rate and the applied stress is not observed in these test, but the thermal loading path affects the creep rate.
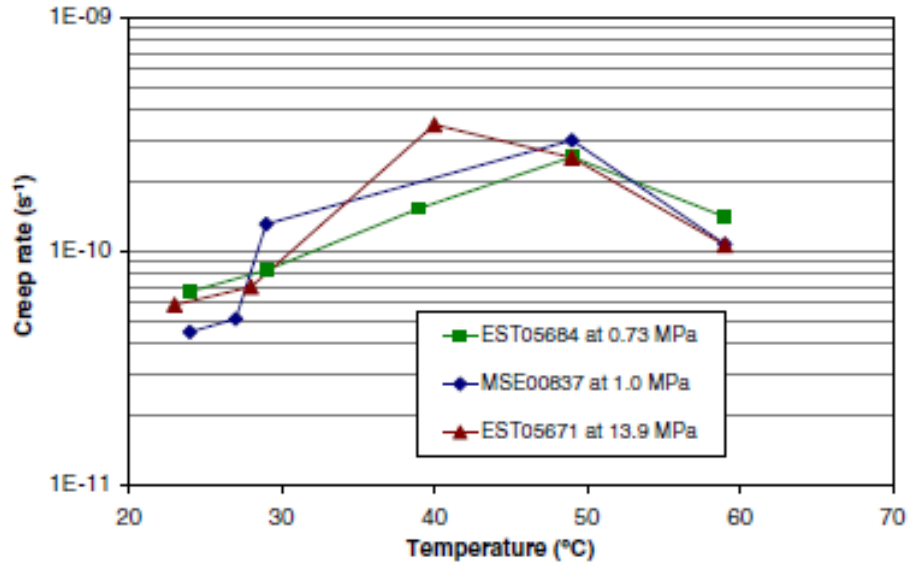
Figure 2.11: Creep rate of Callovo-Oxfordian argillite (Zhang, 2006)

There are two mechanisms which may have caused the increased creep rate during the heating process. The first mechanism results in a reduction of the shear resistance between the particles due to a decreased pore water viscosity, and the second mechanism results in shrinkage due to the pore water release. Since shrinkage is not considered as a creep mechanism, the reduction of shear resistance is considered as the main reason for creep (Cristescu, 1998). However, a high shear resistance might prevent creep due to a large evaporation of the pore water. The creep process is complex and is a result of several factors, but the result from these experiments indicated that the pore water affects the deformation process. The interaction between the clay minerals and the pore water usually initiates at the scale of 1-100 nm, where the causes for self-healing, swelling, creep and failure of the rock originate (Nagra, 2002).

2.4.2 Thermal Impact on Shale Deformation

When shale undergoes a heating process it may experience an irreversible compaction process where the stress history of the shale is of great importance (Bauer, 2014). Figure 2.12 depicts a tri-axial test on a Pierre shale which exhibited similar THM behaviour as the Opalinus clay. Each time the temperature increased, there was an expansion in radial and axial direction followed by a

17

compaction period. Pore pressure equilibration was most likely the reason for the compaction of the sample. A temperature increase caused a higher pore pressure due to the heated water expanded more than the rock matrix and the low permeability of the shale caused the pore fluid to drain slowly. At temperatures higher than 80 degrees Celsius, the poroelastic effects disappeared since the sample mainly compacted during higher temperatures. When the temperature of the sample reached 100 degrees Celsius, the compaction increased vastly without any stabilization period afterwards. The sample was then cooled down to room temperature, this resulted in a smaller compaction rate. These observations of how the temperature varied with the strain rate indicates that there is a relationship between them. Another observation was the anisotropic behaviour of the sample compaction, the shale compacted more in the axial direction than in the radial direction. This is expected due to the anisotropic characteristics of shale. After the experiment was finished, the sample had contracted by 6,5% from its original volume and reduced its porosity by approximately 6,5% (Bauer, 2014).
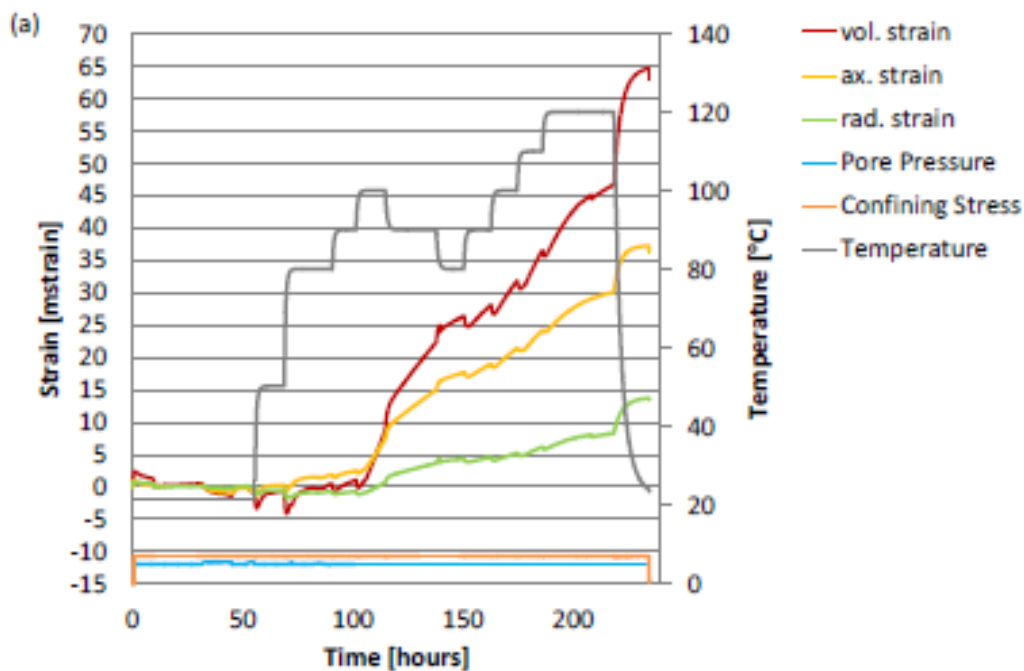
Figure 2.12: Results of the first Pierre shale test (Bauer, 2014).

Figure 2.13 depicts another test conducted on the Pierre shale with only a single temperature increase, the temperature was kept constant at 120 degrees Celsius for approximately 33 hours before it was cooled down. Some of the same characteristics was seen in the second test as in the first, for example the sudden dilation when the temperature increased, followed by compaction. A

creep behaviour could be seen while the temperature was kept constant over a longer time. The three creep stages can be identified when analysing the strain rate. In the tertiary creep phase, the effect of rock hardening makes the strain rate decrease towards the end of the test.
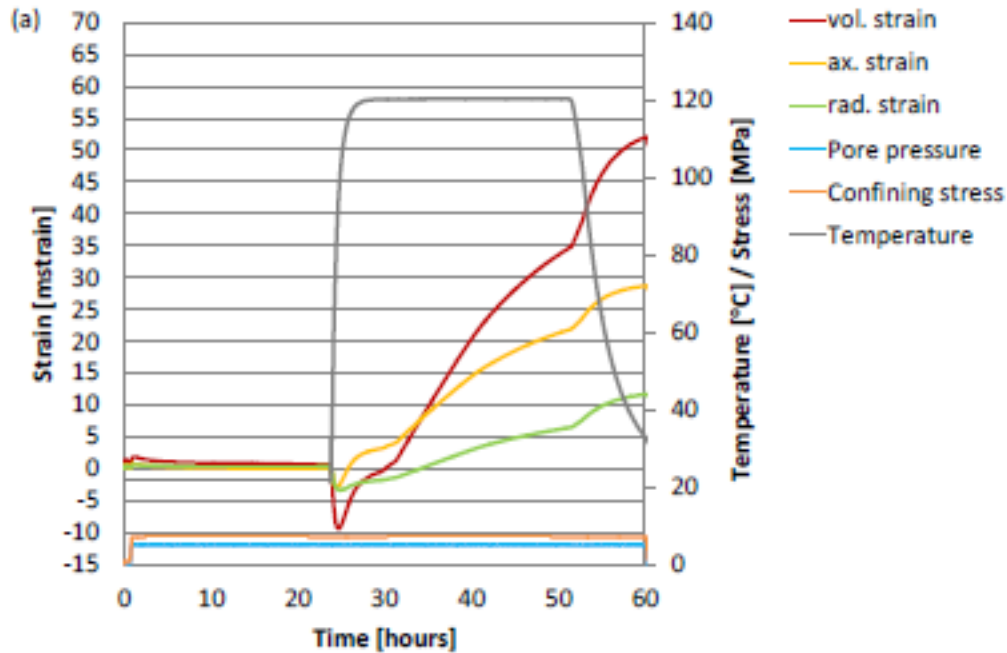
Figure 2.13: Results of the second Pierre shale test (Bauer, 2014).

The shales that were tested went through an irreversible thermally-induced compaction. The creep rate tend to increase with increasing temperature, especially if microscopic processes are involved. These processes which are at an atomic level can explain thermally-induced compaction in normally consolidated shales. The thermally-induced compaction in overconsolidated shales is less since they have previously been exposed to higher stresses and temperatures (Bauer, 2014).

Plastic rock deformation occurred in the overconsolidated shale samples during the heating process. A probable cause for this is due to damaged core samples since stress is relieved from the core sample when it is retrieved from its original in-situ stress state. This may inflict small fractures to the core sample which might not close when the sample is brought back to its original in-situ stress regime in the laboratory. The temperature increase might have led to self-sealing of the fractures in the sample. Another reason for the plastic rock deformation might have been the artificial pore fluid that the sample was exposed to during the laboratory test, where the composition was different from the original pore fluid. This could cause swelling of the shale, which makes it more prone to compaction during heating. The heating rate could also have been

19

crucial for the thermally-induced compaction of the shale samples. After each temperature increase, the samples expanded rapidly before the compaction commenced. This indicates that the pore pressure did not reached equilibrium due to the rapid temperature increase. The pore pressure may have increased vastly if the shale was fully saturated under undrained conditions. This could have caused rock failure if the pore pressure became larger than the total stress, which results in compaction and weakening of the shale.

Irreversible compaction have been seen in shale samples that have been under constant stress and exposed to heating. The possible reasons for the compaction might be the different fluid composition between the original reservoir fluid and the fluid that was used in the laboratory, the high heating rates and a damaged core. All these factors may affect the borehole stability and the cap rock integrity, which means that thermally-induced compaction of shale is important.

The thermally-induced volume change of shale affects its strength since thermally compacted shales have higher shear stresses. The temperature increase leads to an increase of the shear stress, and the distance between the grain particles becomes larger due to the reduction of the attractive forces. This is causing the shale structure to densify until enough bonds are available to withstand a higher effective stress (Xu, 2011). The thermal history of the shale is important when determining its mechanical behaviour. The heating rate which the shale have been exposed to is crucial for its shear strength, Young's modulus and deformation behaviour (brittle or ductile). Figure 2.14 depicts how the heating rate affected the normalized peak strength of some shales. In general, low permeable rocks such as shales only increases their shear strength with a slow heating rate. A slow heating rate minimizes the probability of generation of cracks and excess pore pressure inside the shale. Higher heating rates may decrease the shear strength due the presence of cracks and an uneven distribution of excess pore pressure. Young's modulus increased with increasing temperature and effective confining pressure during the slow heating rate (Xu, 2011).
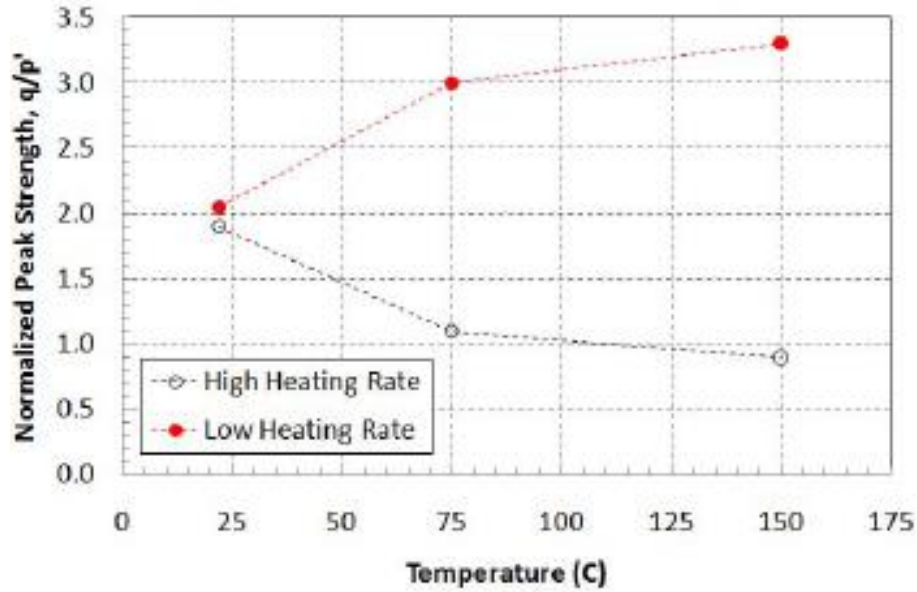
Figure 2.14: Heating rate effects on the mechanical strength of shales (Xu, 2011).

The rate of temperature increase implicates the failure behaviour and the deformation of the shale. Therefore, a rapid temperature increase might lead to crack initiation, while slow heating rates enhances the stability of the shale.

2.4.3 Dehydration of Interlayer Water

The hydration state of a clay is mainly controlled by the smectite layer charge and the salinity of the of the pore fluids (Colten-Bradley, 1987). Smectites in compacting shales expels water at three different temperature ranges, where the third water layer displaces at the lowest temperature range. The temperature range of the first, second and third water layer are expected to be around 160, 70 and 50 degrees Celsius respectively. The dehydration temperatures increase with interlayer density and pore fluid pressure. These temperature ranges are similar to the initiation of hydrocarbon generation and smectite-to-illite transformation (Colten-Bradley, 1987).

Figure 2.15 depicts two geothermal-effective stress gradients which are plotted against pressure-temperature-dehydration curves. Since interlayer water have a range of density values, two values were chosen based on experimental results to represent the dehydration curves. The shaded areas depicts where the loss of the three interlayer water might occur.

21
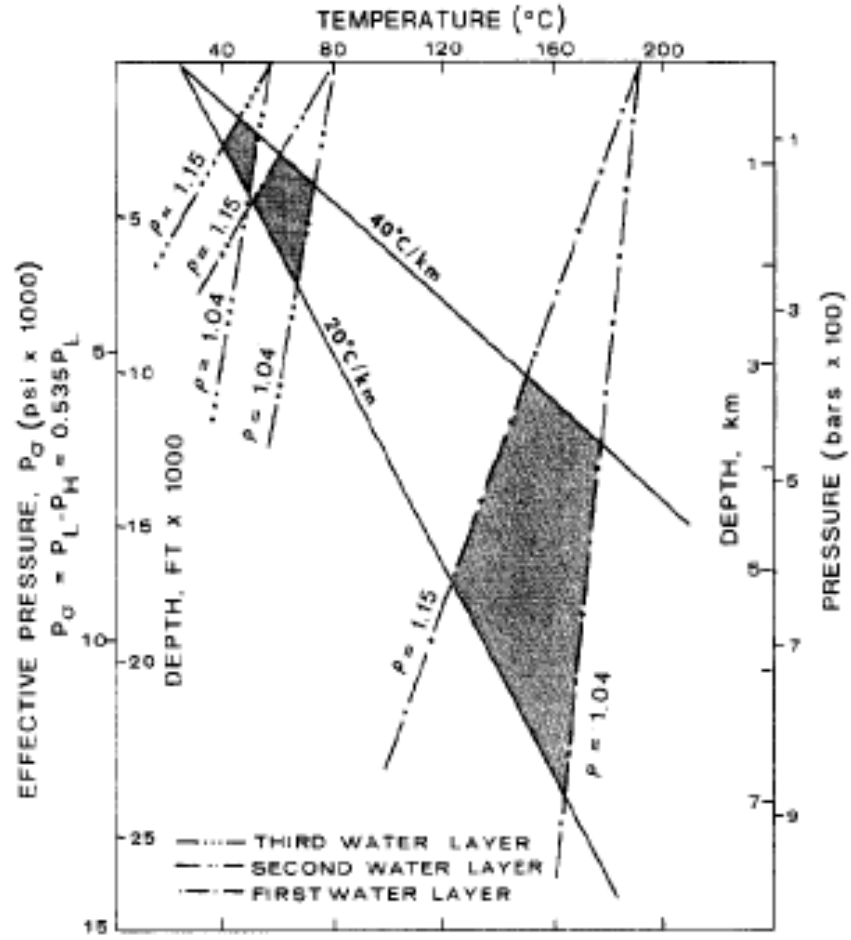
Figure 2.15: Geothermal gradients plotted against pressure-dehydration curves (Colten-Bradley, 1987)

3 Experimental Apparatus and Methods

3.1 Setup

The experiments on the Pierre shale core samples were conducted using a mechanical loading frame and an oedometer test. The principle of the apparatus is very simple. The axial stress acting on the core sample increased when weights were added. Maximum axial load was approximately 30 kN. The core sample was placed between two steel pistons which fitted inside of the steel cylinder, also known as an oedometer cell. Under the lower piston there was a loading cell to record the applied axial load. Above the upper piston there were a linear variable differential transformer (LVDT) to detect the axial displacement of the core sample and several steel cylinders in order to fit the loading frame setup. In addition to these instruments there were temperature sensors, a temperature control element, a pump system and a sensor carrier demodulator. These instruments were connected to an 8-channel universal amplifier called QuantumX MX84A from HBM which was connected to the computer. The readings were gathered using a software called Catman AP (V 4.1.2).

Figure 3.1: The experimental setup

3.2 Equipment

The main components that were used during the experiment is described in detail in the following sections. Some of the sources of error might be inaccurate measurements of the core samples, noise which affected the readings, heat loss through the steel, shorting circuits, varying temperature, leakage, heating of the strain gauges etc. The sampling rate was set to 10 seconds, and 2 seconds when permeability tests were conducted.

3.2.1 The Core Samples

The two cores were Pierre shale from an open cut mine in Colorado in the United States of America. The core samples were prepared to fit inside the hollow steel cylinder and between the two pistons. Thus, they were cut to approximately 4.1 cm in height and 3.8 cm in diameter. The measurements of the samples were taken by using a digital sliding caliper. Four measurements were taken to determine the diameter, two perpendicular measurements at the top and bottom of the cores. The heights were found by taking two perpendicular measurements. Each core was placed on a digital weighing scale in order to determine its weight. The accurate measurements and petrophysical properties of the core samples can be found in the Appendix. The core samples were saturated and stored at room temperature prior to the experiment. The cores had bedding planes perpendicular to the applied axial load direction.

Figure 3.2: Core sample 1

3.2.2 Steel Cylinder and Pistons

The thick walled steel cylinder had a height of 8 cm, an inner radius of 19.15 mm and an outer radius of 44.15 mm. The pistons had a slightly smaller radius than the inner radius of the cylinder in order to avoid leakage. Two porous plates were placed between the core sample and the pistons

to ensure an evenly distributed fluid flow. After the lower piston was placed inside of the cylinder the core sample was placed on top of it and the cylinder was filled with fluid before the upper piston was placed on top of the core sample.

Figure 3.3: Thick walled cylinder, lower piston and a sketch of a thick walled cylinder (Daly, 2003)

3.2.3 Strain Gauges

Four strain gauges were attached on the outside of the thick walled cylinder using glue. Figure 3.3 depicts where the strain gauges were positioned, with 90˚ spacing and in the centre of the cylinder. In order to obtain data from these strain gauges, wires and cables had to be made to connect the strain gauges to the 8-channel universal amplifier. The first step was to scratch 16 copper wires in both ends to ensure good connectivity, and solder them to each solder tab area on the strain gauge using lead. The strain gauges on opposite side of each other were connected in pairs by soldering the copper wires together in a certain order with respect to their excitation and signal, depicted in the Figure 3.4. Two cables were peeled in both ends, inside the cables there were 4 wires (red, white, black and green) which were soldered to the copper wires in the one end. The red wire was soldered to number 1, the white wire to number 2, the black wire to number 3 and the green wire to number 4.

1: + signal

2: - excitation

3: - signal

4: +
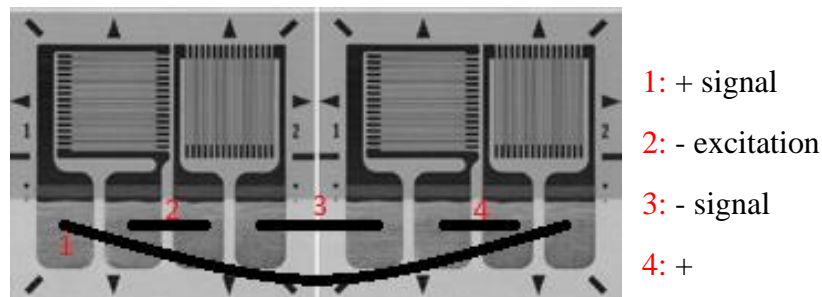
Figure 3.4: Sketch of how the strain gauges were connected in pairs (Micro Measurements, 2015)

The connections were isolated with rubber to avoid any disturbances. The rubber shrunk onto the soldering connection when heat was applied using a heat gun. The wires was attached to the steel cylinder to ensure stability. In the other end of these two cables a transducer connection was used. A full bridge connection for strain gauges was used when the cables were soldered, a sketch can be found in the Appendix. The strain gauge pairs were connected to separate channels in the 8-channel universal amplifier, as depicted in Figure 3.5. Thus, two strain gauge measurements were taken.

Figure 3.5: Thick walled cylinder with strain gauges and the 8-channel universal amplifier

3.2.3.1 Working Principle

The strain gauges was a product of Micro-Measurements and are called CEA-06-125UT-120. A single strain gauge consist of two-element 90 degrees tee rosette and four soldering tab areas, shown in Figure 3.4. The specifications of the strain gauges can be found in the Appendix. The steel cylinder deforms when the internal pressure and temperature changes, and alters the grid area of the strain gauges. This causes a change in the electrical resistance, which can be transformed to a strain measurement according to Equation [1] since the gauge factor and resistance of the grids are known (Micro Measurements, 2015).

$$\varepsilon = \frac{\Delta R}{GF * R_0} \qquad\qquad [1]$$

Where ε is strain, ΔR is change in the electrical resistance, GF is the gauge factor and R_0 is the grid resistance. The strain gauges were calibrated to measure pressure.

3.2.4 Loading Cell

The cable that connected the loading cell to the 8-channel universal amplifier was prepared similar to the strain gauge cables. Instead of soldering the four wires in the one end to copper wires, they were soldered to a four pin connector which could be connected to the loading cell. Equation [2] could be applied to determine the applied force and stress on the core sample, but the loading cell was used to record it digitally in order to get a more accurate measurement.

$$\sigma = \frac{F * F_{mech}}{A} = \frac{4mgF_{mech}}{\pi d^2} \qquad\qquad [2]$$

Where σ is stress acting on the core sample, F is applied force, A is the cross-sectional area of the core sample and F_{mech} is a factor that represents the mechanical loading frame setup and has a value of 10. The calculations can be found in the Appendix.

3.2.5 The Pump System

The pump used was a Quizix QX series, a product of Chandler Engineering. The pump was controlled from Quizix's software program PumpWorks. The pump usually maintained a constant pore pressure of 2 MPa using brine with 3.5% NaCl, which is similar to seawater. The brine was transported through steel tubes from the brine container to the core sample. A transient permeability apparatus was included in the system in order to make permeability tests of the core samples, depicted in the Figure 3.6. The tests were conducted by cutting the fluid supply to the cores, altering the differential pressure and measure how long time it took for the differential pressure to reach equilibrium.
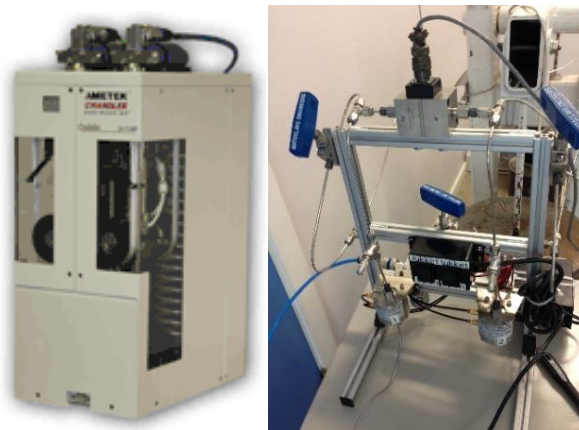
Figure 3.6: The pump and the transient permeability apparatus

3.2.6 Sensor Carrier Demodulator

An amplifier called Validyne CD15 General Purpose Basic Carrier Demodulator was used to measure the differential pressure in the core sample. It was connected to the transient permeability apparatus and provided a direct current output signal.

Figure 3.7: The sensor carrier demodulator

3.2.7 Linear Variable Differential Transformer (LVDT)

One LVDT was used during the experiments. It was mounted above the upper piston in such a way that it could record the axial displacement of the core sample. The LVDT mainly consist of the rod, core and the body. The body was attached above the upper piston, while the rod and core rested on the steel cylinder. When the upper piston and the body were moving in axial direction, the core measured the displacement.
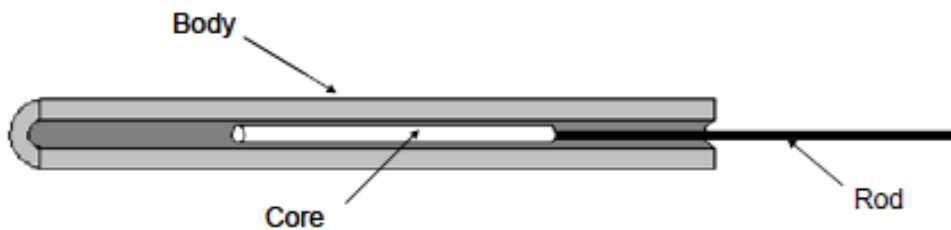
Figure 3.8: Sketch of a LVDT (Ubilla, 2007)

3.2.8 Temperature Sensors

There were two temperature sensors, one measured the room temperature while the other sensor measured the inflicted temperature on the core sample. The latter temperature sensor was not connected to the 8-channel universal amplifier, but to Pico Technology TC-08 USB logger. This logger was plugged directly into a USB-port on the computer and PicoLog software was used to collect data. It also had 8 channels, but only one of them was used. The channel was used to log the temperature outside of the heating element. The heating element was simply placed and taped

around the steel cylinder, depicted in the Figure 3.9. The tape had a maximum limitation of 150 degrees Celsius. The heating element was connected to a control element which was not linked to the computer, depicted in the Figure 3.9. The control element varied the heat supply to the heating element based on its programmed temperature limitations, it had its own temperature sensor which was also placed on the outside of the heating element. A layer of temperature isolation was placed and taped outside of the heating element to minimize the heat loss.

Figure 3.9: The heating element with and without temperature isolation and the control element

The uncalibrated accuracy of the temperature readings is a sum of $\pm 0.5°C$ and $\pm 0.2\%$ of the measured temperature (Pico-Technology, 2013). At 80°C this might result in a 0.9°C deviation at the most, which is acceptable.

3.3 Calibration of the Equipment

The pump system was calibrated by running paraffin through it to check for leakage or air bubbles, and to check that the pressure data corresponded with the pump pressure. Afterwards the fluid was replaced by brine with 3.5% NaCl, since brine is the most common pore fluid (Wang, 1992). The LVDT was calibrated using a calibration device from Mitutoyo. Figure 3.10 depicts the apparatus that was used to calibrate the strain gauge measurements and the loading cell. The loading cell was simply calibrated by applying a certain amount of weight onto it, and adjusting the digital measurement. Since the applied heat disturbed the strain gauge readings, it had to be accounted for. This calibration process was conducted by filling the cylinder with brine and increase the temperature in several steps to record how the strain gauge measurements altered with temperature. Each temperature step lasted until the strain gauge measurements had stabilized, before the next

29

heating period commenced. An average of the last recorded data points before the next heating period were used to determine the correction factors for the strain gauge measurements, the calculations can be found in the Appendix.

Figure 3.10: Calibration equipment

3.4 Experimental Methods

There were some aspects that needed to be taken into consideration regarding the experiment, for instance how the fluid viscosity altered with temperature and how the permeability was measured.

3.4.1 Viscosity and Density of the Fluid

Fluids are considered incompressible due to a negligible change in viscosity and density with increasing pressure, but the temperature dependency has to be accounted for in the calculations since the viscosity and density decreases with increasing temperature. The salinity content of the fluid is also of importance since it increases the viscosity and density of the fluid, especially at temperatures below 100˚C (Wang, 1992). The applied heat is assumed to affect the fluid almost immediately due to the high thermal conductivity of steel (Peet, 2011).

3.4.1.1 Dynamic Viscosity

Determining the viscosity of water with increasing temperature can be calculated by using Equation [3], where μ is dynamic viscosity, T is absolute temperature, a, b and c are experimentally constants (Cimbala, 2006). The constants can be used for water since they result in an error less than 2.5% in viscosity in the temperature range 0˚C-370˚C (Touloukian, 1975). The calculations can be found in the Appendix.

$$\mu = a10^{(b/(T-c))} \tag{3}$$

Since Equation [3] do not include the salt concentration of the fluid, Equation [4] can be applied. Equation [4] is an approximation for brine viscosity for temperatures below 250˚C, where μ is viscosity, S is the weight fraction of NaCl and T is the temperature of the fluid (Wang, 1992).

$$\mu = 0.1 + 0.333S + (1.65 + 91.9S^3)exp\{-[0.42(S^{0.8} - 0.17)^2 + 0.045]T^{0.8}\} \tag{4}$$

Figure 3.11 depicts the dynamic viscosity of brine in its liquid phase at 1 atm between 20-100˚C.
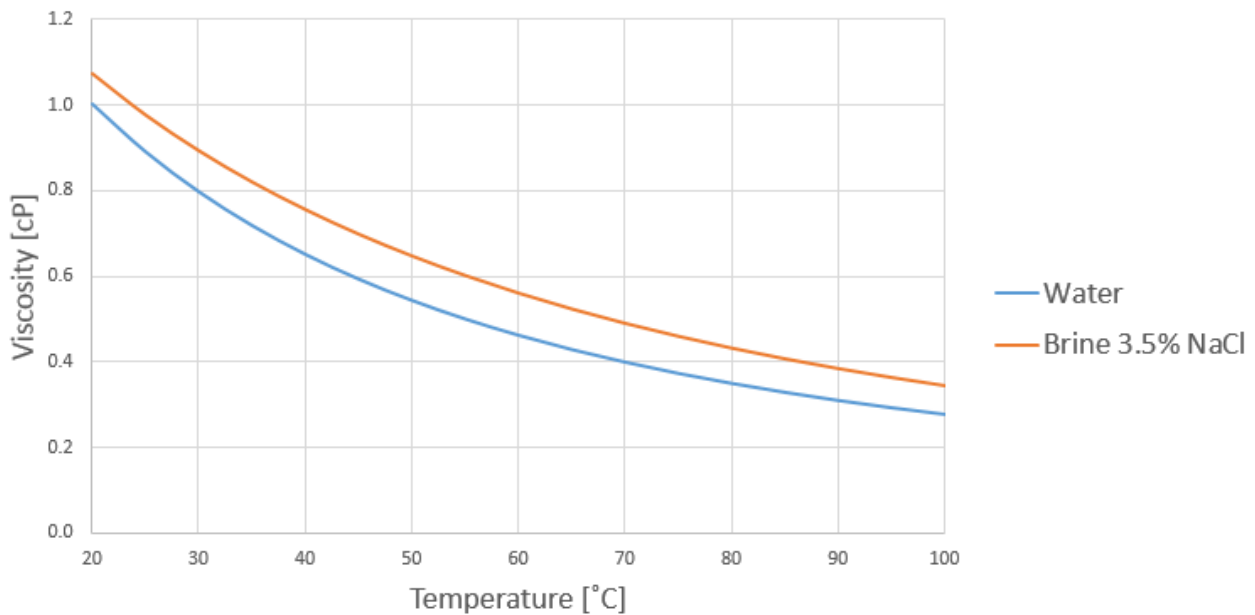
Figure 3.11: Dynamic viscosity of brine

If Equation [4] is applied to calculate the dynamic viscosity of water, the result is almost identical as the result Equation [3] provides. This relationship increases the credibility of the brine viscosity approximation. The calculations can be found in the Appendix.

3.4.1.2 Density

The change in the water density with temperature can be expressed by applying Equation [5] and [6], where $\rho_{w,1}$ is the water density before the temperature increase, $\rho_{w,2}$ is the water density after the temperature increase, β is the volume expansion coefficient and ΔT is the temperature change (Cimbala, 2006). Calculations can be found in the Appendix.

$$\Delta\rho_w = -\beta\rho_{w,1}\Delta T \qquad\qquad [5]$$

$$\rho_{w,2} = \rho_{w,1} + \Delta\rho_w \qquad\qquad [6]$$

The brine density with increasing temperature is approximated by Equation [7], where ρ_w is water density, ρ_{brine} is brine density, S is the weight fraction of NaCl and T is the temperature of the fluid (Wang, 1992).

$$\rho_{brine} = \rho_w + S\{0.668 + 0.44S + 10^{-6}[T(80 + 3T - 3300S)]\} \qquad [7]$$

The same trend is observed for Equation [7] as for Equation [4] with respect to its credibility and is therefore applied. Figure 3.12 depicts the fluid density of water and brine with 3.5% NaCl.
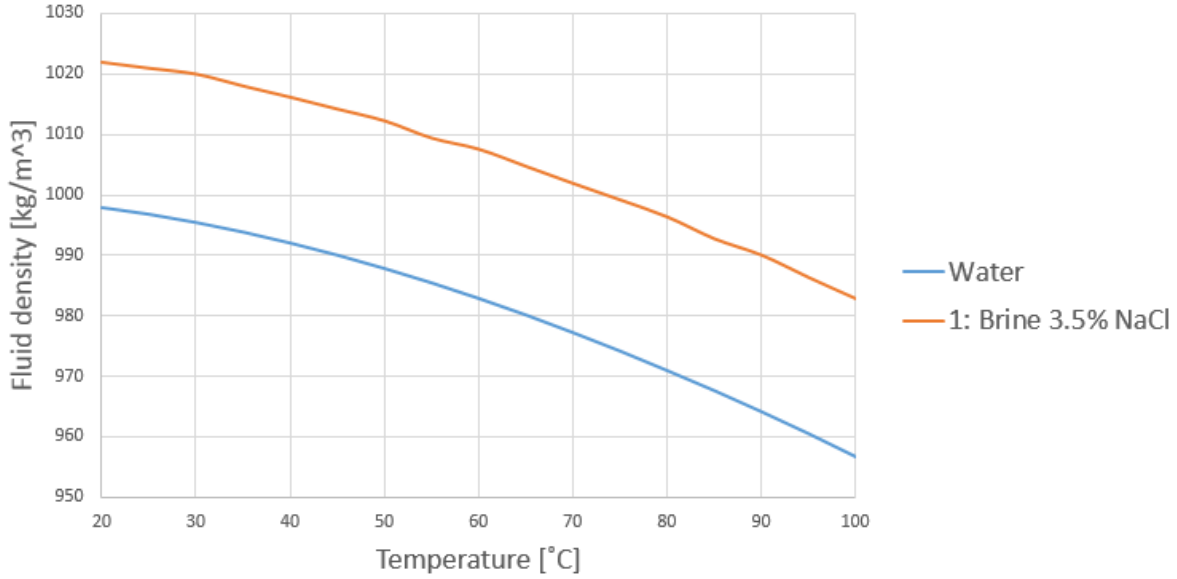
Figure 3.12: Fluid density of brine

3.3.2 Permeability

Permeability measurements are of interest during the creep process in order to observe how the axial permeability of the core sample alters as it compacts. If a selected shale section is supposed to create a sealing annular barrier, it is important that the shale do not lose its sealing properties after it have dilated onto the casing. The permeability tests were conducted by closing the valves on the transient permeability apparatus, which created a closed system inside of the oedometer cell. An axial pressure difference was created by using valves on the transient permeability apparatus. The exponential differential pressure decline was recorded as a function of time as the differential pressure equalized. The axial permeability of the core samples was calculated by using Equation [8].

$$k = \frac{\mu * h_{core} * \alpha}{2 * A * K_m} \qquad [8]$$

Equation [8] is an experimental method for determining the permeability, where k is permeability, μ is dynamic viscosity, h_{core} is the height of the core when the permeability test is conducted, α is the exponential decline factor which was obtained from the trendline of the permeability tests, A is the area of the core sample and K_m is a constant for the experimental setup.

33

3.4.3 Thermal Expansion of the Oedometer Cell

The oedometer cell and the equipment were affected by the temperature increase caused by the heating element, this caused the steel alloys to expand. This affected the LVDT readings, and increased the axial displacement rate readings during the heating periods. Therefore, this should not be interpreted as an immediate thermal effect on the axial displacement of the core sample.

3.4.4 Calibration of Strain Gauges

The strain gauges were not calibrated for temperature, this had to be corrected in order to use the strain gauge measurements. Therefore, a calibration process was conducted with only brine inside of the thick walled cylinder and varying temperatures. Figure 3.13 depicts the temperature and strain gauge measurements correlation.
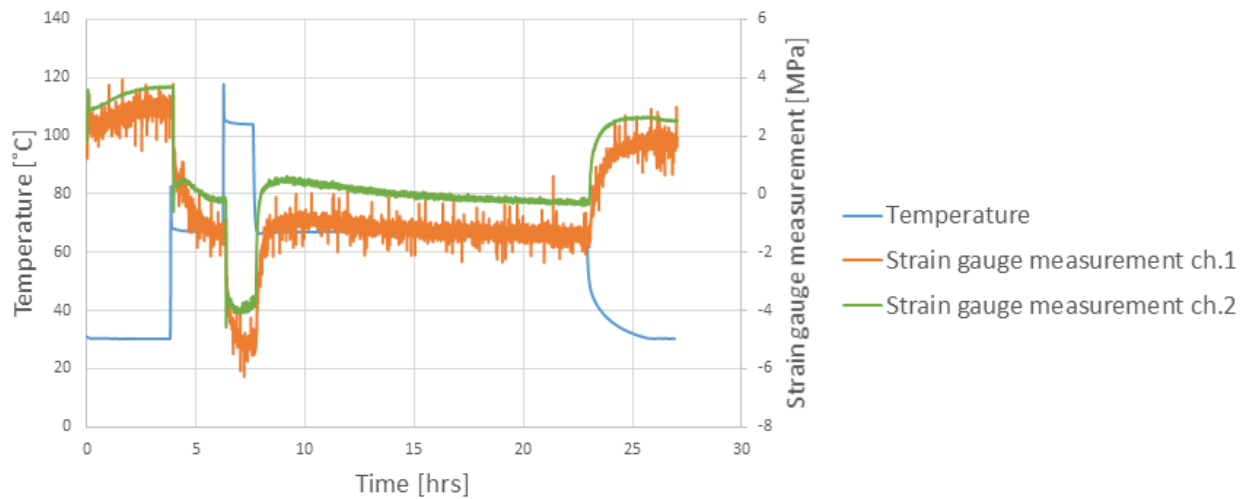
Figure 3.13: Correlation between the temperature and the strain gauge measurements

The temperature steps were 30˚C-65˚C-100˚C-65˚C-30˚C. The calibration was conducted at the end of each temperature step, when the measurements had stabilized. Figure 3.14 depicts four data points which represents each temperature step, where the slope determined the correction factor. The correction factor for the strain gauge measurements of channel 2 was -0.0863 and -0.9321 for the strain gauge measurements for channel 1.
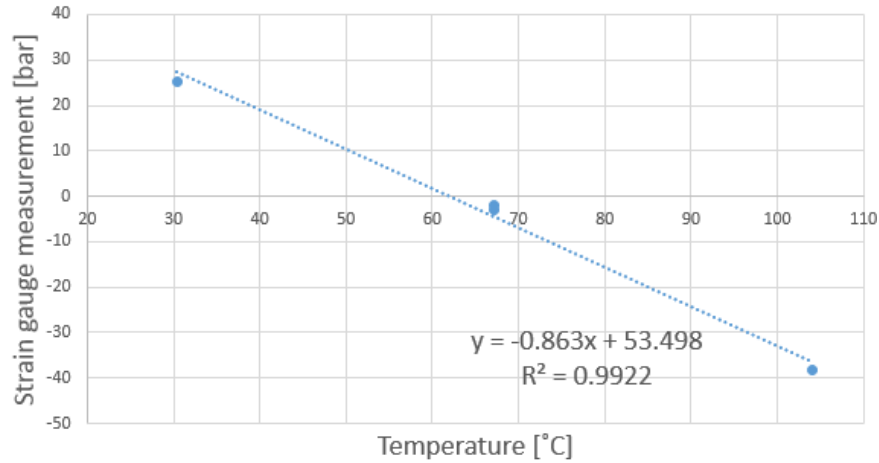
Figure 3.14: Correction factor for the strain gauge measurements of channel 2

The corrected strain gauge measurement was calculated by using Equation [9], where ε_{corr} is the corrected strain gauge measurement, ε_{mea} is the measured strain gauge measurement, F_{corr} is the correction factor and ΔT is the temperature change.

$$\varepsilon_{corr} = \varepsilon_{mea} - (F_{corr} * \Delta T) \qquad [9]$$

Figure 3.15 depicts the strain gauge measurements after calibration. The correction was applied to the strain gauge measurements of the second core sample.
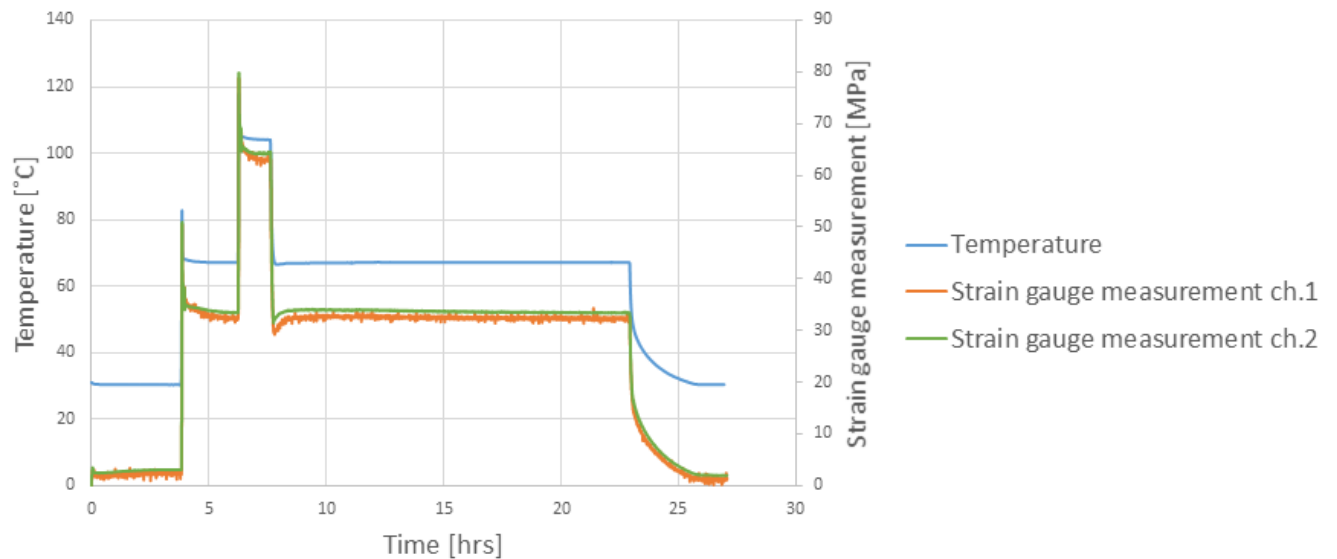
Figure 3.15: Corrected strain gauge measurements

3.5 Risk Assessment

A risk assessment had to be conducted before the experiment could start in order to identify and mitigate the risks, as shown in Table 3.1.

Hazards	What may happen?	Likelihood	Consequence	What can mitigate the risk?
Pressurized air	Hoses may loosen from the mounting point to the pump	Low	Low	Check all mounting points and hoses. Check if the pump receives a steady flow
Weights	Drop them on the feet	Low	Low	Work slow and steady, use protective footwear
Fluid pressure	Leakage may create small ponds on the floor which may cause people to slip, and brine may damage the apparatus	Medium-high	Medium	Check that the cumulative volume is constant. Thorough check of the system, lubricate O-rings, tighten screws. Use protective goggles and clean up the fluid
Heating element	Shorting circuits may cause a fire.	Low	High	Pay extra attention when heating, have a fire extinguisher nearby
People	Other people may disturb the experiment	Low	Medium	Put up a sign that states that an experiment is ongoing, do not touch
Soldering	Burn marks or inhale the fumes from the lead	Medium	Low	Proper equipment, take precautions, use suction outlets

Table 3.1: Risk Assessment Matrix

4 Experimental Results

Two Pierre shale core samples were tested for approximately two weeks in order to observe the creep behavior and the permeability. The applied stress was relatively low, which implied an occurrence of only the primary creep phase. Creep rate was investigated at different temperatures. The experiment was uniaxial until the sample expanded and touched the wall. Afterwards, it gradually transferred to a uniaxial strain path. Axial strain was measured during the permeability tests. Fluid volume was obtained from the pump data, the annulus fluid was brine with 3.5 % NaCl. Strain gauges were placed on the outer wall of the thick walled cylinder to assess the horizontal stress. Finally, axial permeability was measured at different stages of the test.

4.1 The First Core Sample

The first test was characterized as a learning process of how to obtain proper data from the experimental setup, for instance this led to technical problems and inaccuracies in the permeability tests. Temperature deviations and leakage was some of the problems which occurred, the physical proof of leakage can be seen in Figure 4.1 where NaCl was found on top of the loading cell after the test was conducted.

Figure 4.1: The first core sample and salt on top of the loading cell

Figure 4.1 depicts the core sample after it was removed from the thick walled cylinder. Cracks were observed, which is an indication of increased permeability.

4.1.1 Axial Load

The axial load was increased stepwise by adding weights until desired load was reached, as depicted in Figure 4.2. The applied weights had to be removed during the test due to incorrect setup of the equipment. The arm which the weights were placed onto touched the ground, this resulted in a lowered axial load onto the core sample. This problem was solved by removing all the weights

in order to add a small steel cylinder above the upper piston, this elevated the arm where the weights was placed.
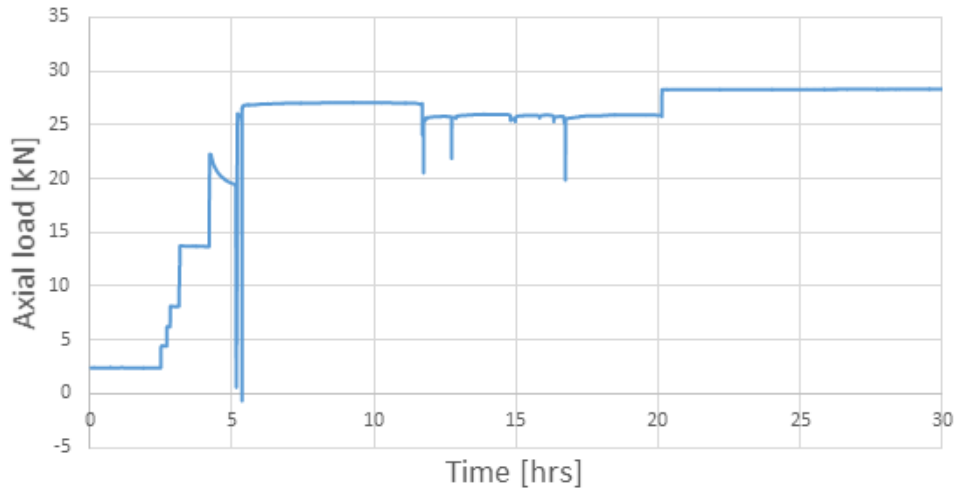
Figure 4.2: Axial loading of core sample 1

4.1.2 Temperature

The core sample was exposed to room temperature until the heating element was attached around the thick walled cylinder after approximately 286 hours. The applied heat fluctuated in the beginning due to incorrect setup of the control element. This resulted in a few degrees Celsius deviation from the planned temperature. Therefore, the settings of the control element was corrected to maintain a stable temperature. Figure 4.3 depicts that the core sample was cooled down at the end of the test, this time interval was not recorded in the other data due to technical problems.
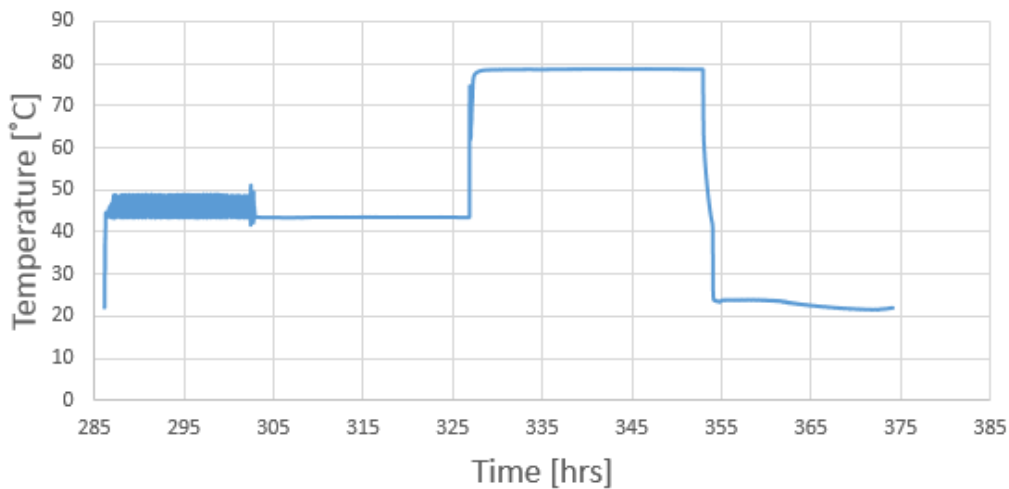
Figure 4.3: Temperature of core sample 1

4.1.3 Axial Displacement

The LVDT measured the axial displacement of the core sample during the test. Figure 4.4 depicts that the core sample compacted almost 2 mm in the axial direction from its original state, especially in the beginning of the test when the axial stress was increased and at the end when heat was applied.
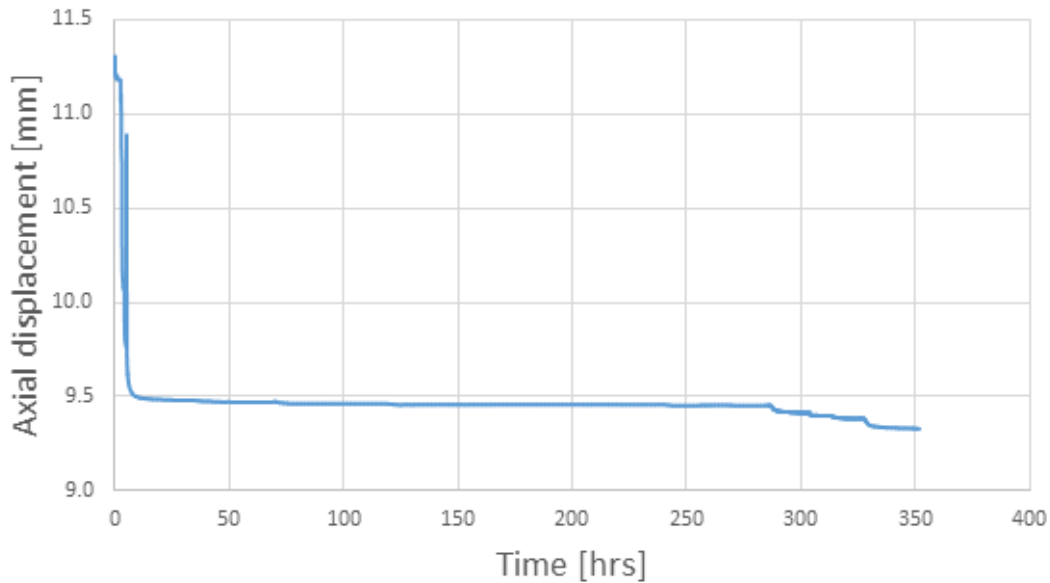
Figure 4.4: Axial displacement of core sample 1

However, due to the presence of different alloys in the experimental setup the temperature increase caused an expansion of the equipment near the heating element which affected the LVDT readings. Therefore, the transient periods after a change in temperature should not be considered for determination of the creep rate. The effect of temperature increase is depicted in Figure 4.5, where the core sample seems to compact rapidly. This was observed in the test of second core sample as well.
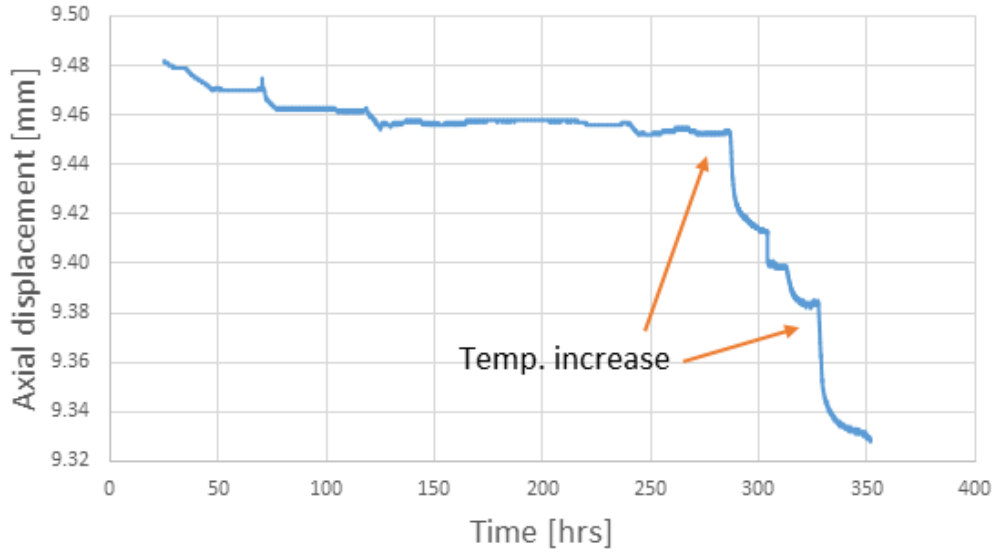
Figure 4.5: Axial displacement of core sample 1 under constant stress conditions

4.1.4 Creep rate

Only the creep rate at room temperature was obtained for the first core sample because the heating periods were too short to obtain a proper creep rate at the elevated temperatures. This can be seen in Figure 4.5, where the heating effect on the LVDT measurements camouflages the creep rate.
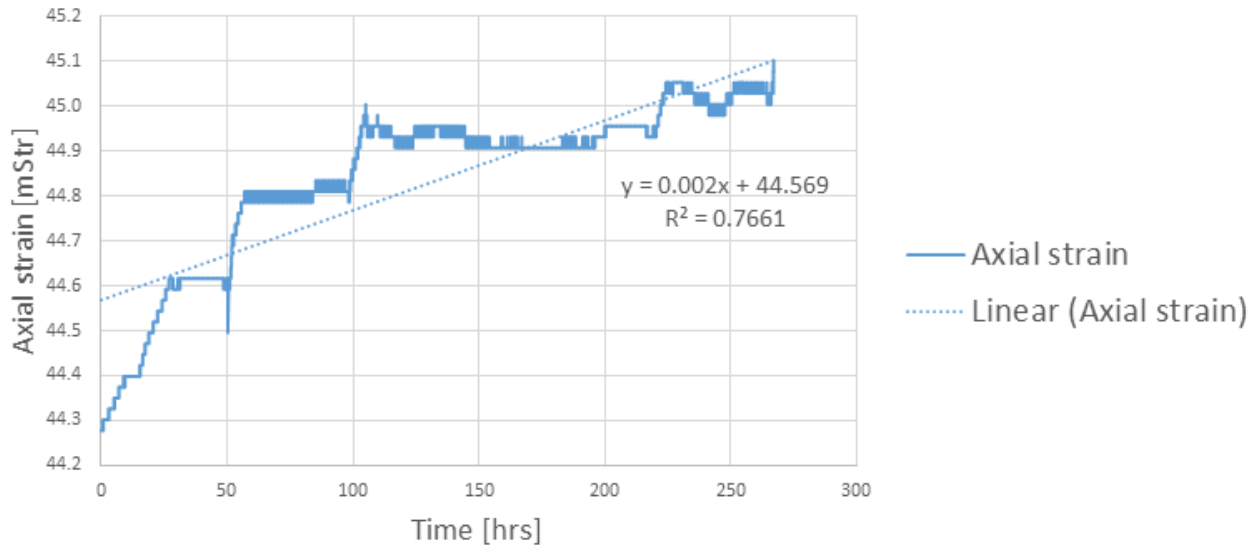
Figure 4.6: Axial strain of core sample 1 at room temperature

Figure 4.6 depicts the axial strain of the first core sample at room temperature, where the creep rate was $0.002\ mStr/hr$.

4.1.5 Pump

Figure 4.7 depicts a slight increase of the cumulative volume of brine during the test, which is an indication of leakage. The pump provided a continuous flow of fluid to the system since it was set to maintain a constant pore pressure of 2 MPa.
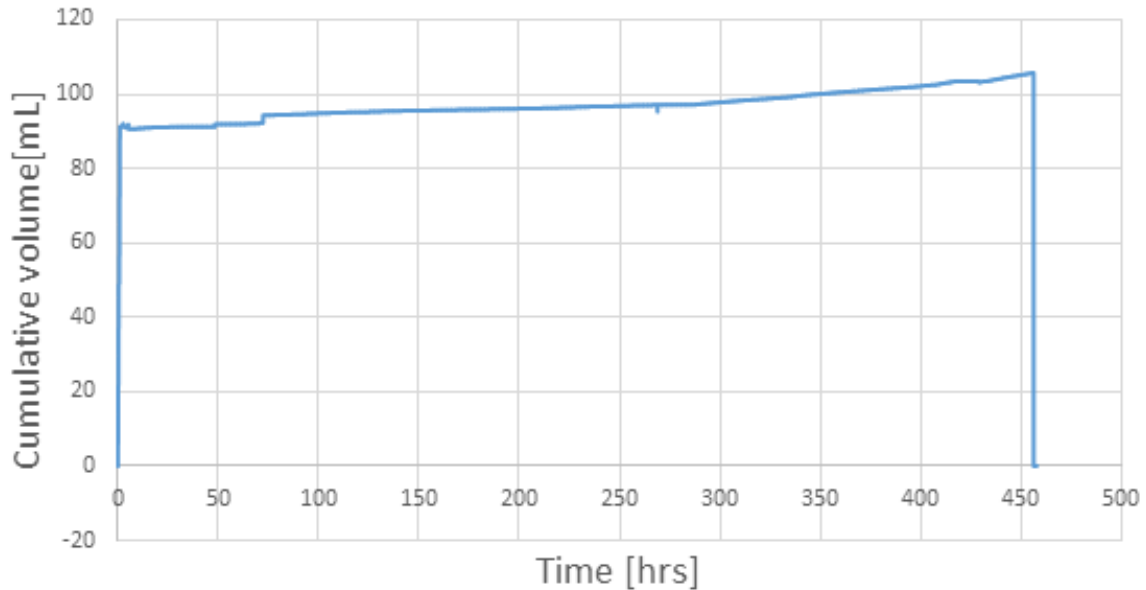
Figure 4.7: Cumulative volume provided by the pump during core sample 1

4.1.6 Permeability Tests

Five permeability tests were conducted in order to determine the permeability of the core sample. The first permeability test was conducted at room temperature, the next two at 50°C and the last two tests were taken at 80 °C. The change in temperature affects the fluid viscosity which had to be accounted for. Figure 4.8 depicts the permeability tests on a logarithmic scale, the tests lasted for approximately 30 minutes until the differential pressure equalized. There were some differences in the initial differential pressure of the permeability tests.
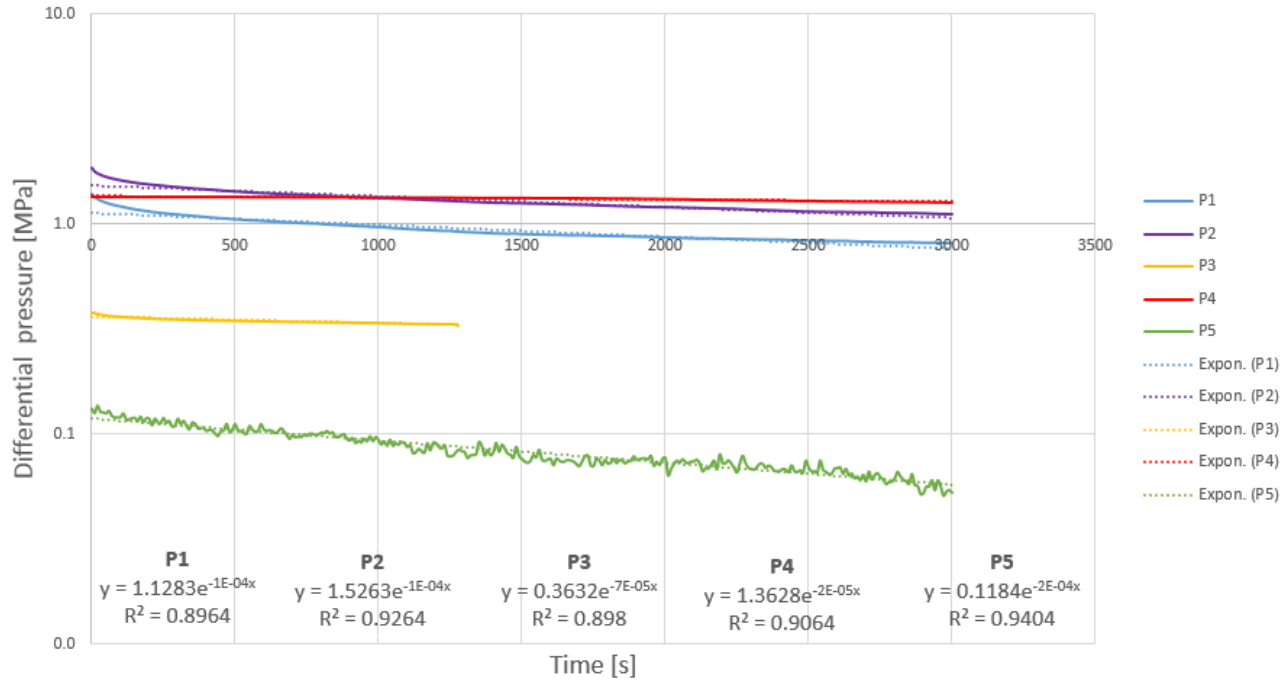
Figure 4.8: Permeability tests of core sample 1

The exponential trendline fit the decline curves of the differential pressure since the R^2 value is close to 1. The α values were obtained from the Equation of the trendlines, for instance for the first permeability test the α value was $\alpha_1 = 1E - 04$ as depicted in Figure 4.8. All the permeability calculations can be found in the Appendix. The leakage probably caused some inaccuracies in the permeability tests, but the impact of the leakage was mitigated by only measuring the differential pressure respond from the upper piston due to leakage in the lower piston. The valve to the lower piston was closed during the permeability tests. This approach resulted in credible permeability values.

Permeability test [#]	Temperature [˚C]	Permeability [nD]
1	23	378
2	50	250
3	50	175
4	80	33
5	80	333

Table 4.1: Permeability measurements of core sample 1

The axial strain was calculated when the permeability tests were conducted by using Equation [11]. Figure 4.9 depicts the increase of the axial strain as the core sample compacted in the axial direction. The data points were obtained from Table 4.1. The axial strain changed with approximately 3.5 mStr.
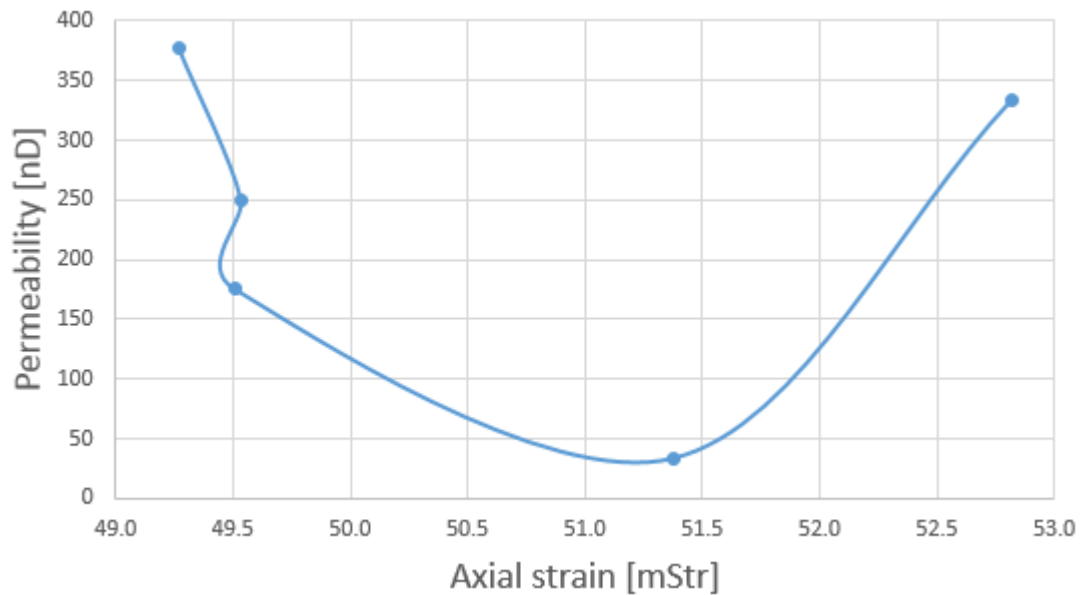
Figure 4.9: Axial strain vs. permeability of the permeability tests of core sample 1

4.1.7 Strain gauge measurements

Most of the strain gauge measurements from the first core sample were obtained, but due to technical problems during the test these were not presented.

4.2 The Second Core Sample

The second core sample was from the same Pierre shale as the first core sample. The steel tube and the coupling which was connected to the lower piston was replaced as a countermeasure for the leakage.

4.2.1 Axial Load

The axial load was increased in 7 steps, as depicted in Figure 4.10. The axial load remained constant after the final increase to approximately 30 kN.
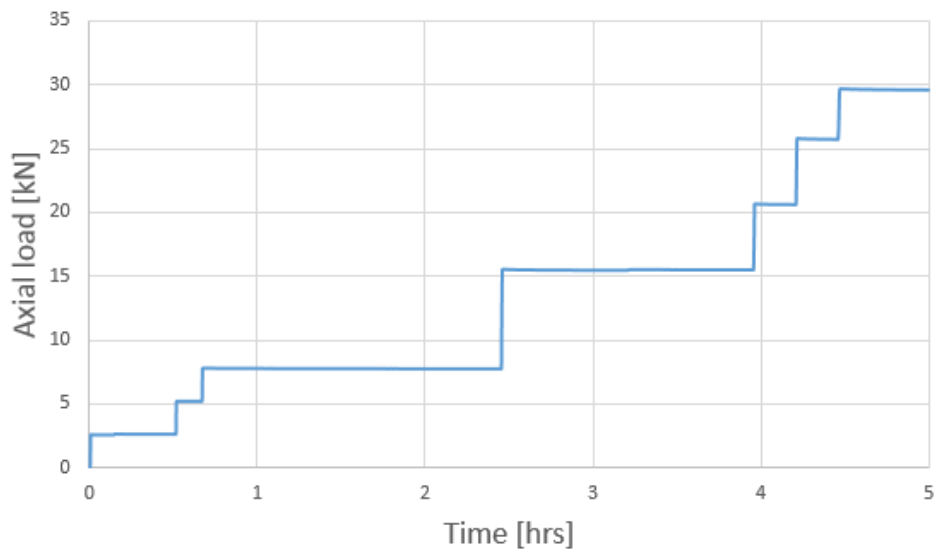
Figure 4.10: Axial loading of core sample 2

4.2.2 Temperature

The core sample was kept at room temperature for one day before the heating periods commenced. The temperature was increased to 50˚C, 80 ˚C, 90 ˚C and 100 ˚C before the core sample was cooled down to room temperature as can be seen in Figure 4.11. The duration of the 50˚C and 80˚C temperature step was longer than the others to check if the displacement of the third and second water layer could be observed.
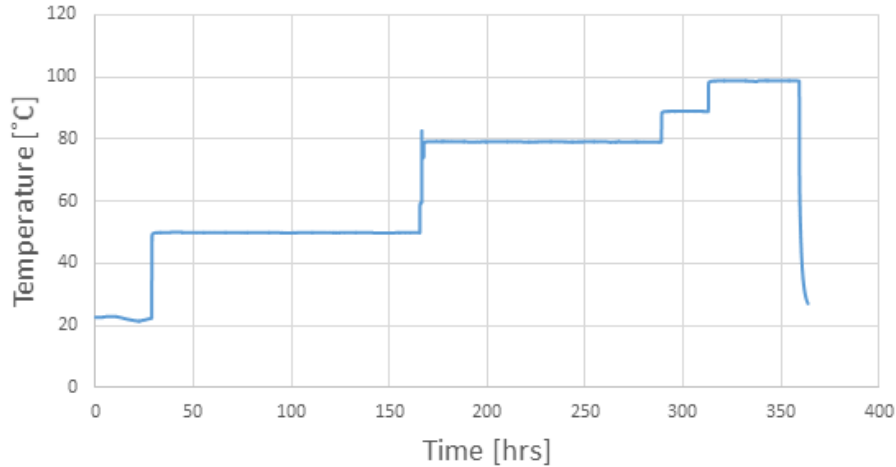
Figure 4.11: Temperature of core sample 2

4.2.3 Axial Displacement

Figure 4.12 depicts the axial displacement of the second core sample which compacted approximately 2 mm, especially in the beginning of the test when the axial stress was increased.
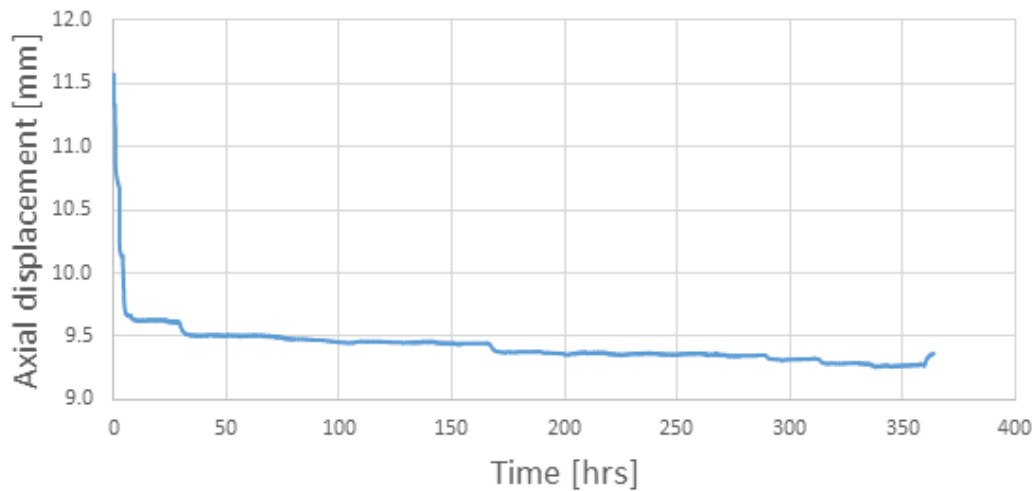
Figure 4.12: Axial displacement of core sample 2

Figure 4.13 depicts the axial displacement of the core sample under constant stress conditions. The change in temperature affected the axial displacement readings. Heating the core sample resulted in compaction in the axial direction, while cooling resulted in expansion in the axial direction. The immediate thermal effect on the axial displacement readings have been discussed, and are not relevant for determining the creep behaviour at elevated temperatures.

45
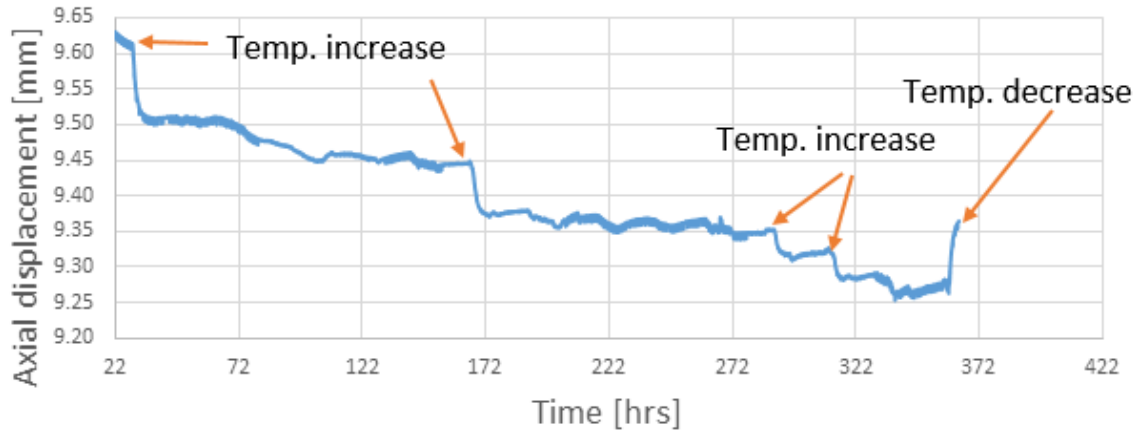
Figure 4.13: Axial displacement of core sample 2 under constant stress conditions

The axial displacement was plotted against axial load and the strain gauge measurements of channel 1 in the beginning of the test at room temperature, as depicted in Figure 4.14.
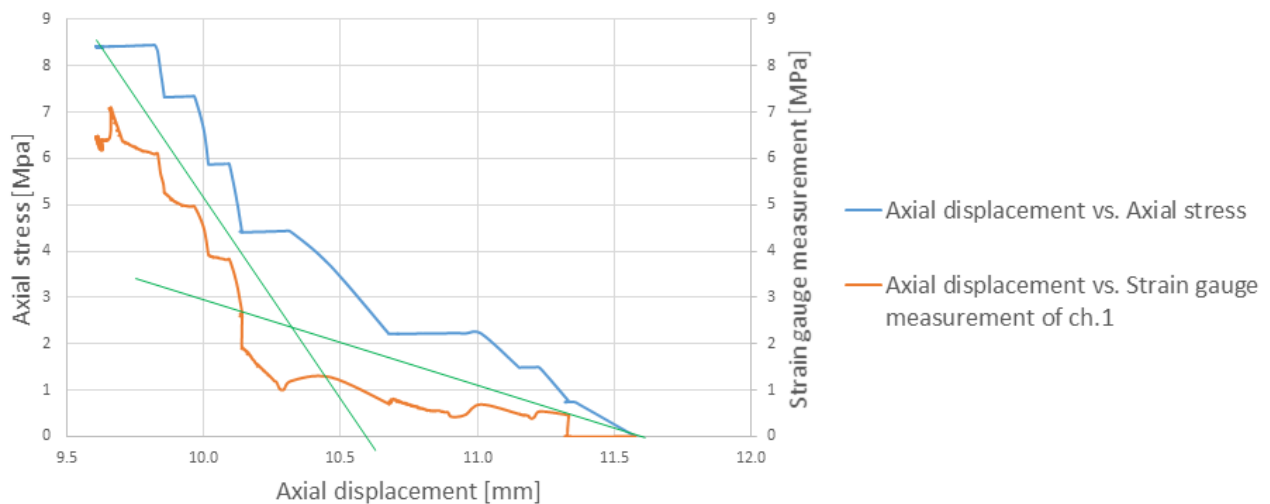
Figure 4.14: Axial displacement versus axial stress and strain gauge measurement of ch.1

The green lines in Figure 4.14 illustrates a significant change of the axial displacement with respect to the axial stress and radial strain, which is an indication of contact between the core sample and the wall. The core sample compressed uniaxial before it reached the wall, the Poisson's ratio (ϑ) during this compression was calculated to be 0.469 by using Equation [10], [11] and [12].

$$\frac{\varepsilon_r}{\varepsilon_z} = -\vartheta \qquad [10]$$

$$\varepsilon_z = \frac{\Delta L}{L} \qquad\qquad [11]$$

$$\varepsilon_r = \frac{\Delta r}{r} \qquad\qquad [12]$$

It is not certain when the core sample failed, but according to the obtained data it might have failed approximately when it reached the wall. After the core sample reached the wall, the stress path transferred from uniaxial compaction to uniaxial compression. The Poisson's ratio for uniaxial compression was calculated by using Equation [14]. The change in axial and radial stress was obtained from Figure 4.14. This resulted in a Poisson's ratio of 0.485, which is almost the same as the Poisson's ratio when the core sample compressed uniaxial. The calculations can be found in the Appendix.

$$\frac{\Delta\sigma_r}{\Delta\sigma_z} = \frac{\vartheta}{(1-\vartheta)} \qquad\qquad [13]$$

$$\vartheta = \frac{\Delta\sigma_r}{(\Delta\sigma_r + \Delta\sigma_z)} \qquad\qquad [14]$$

The stiffness of the core sample during uniaxial compression and uniaxial compaction can be compared by applying Equation [15] and [16], where the Young's modulus (E) is a measure of the stiffness of the core sample. Equation [15] represent uniaxial compression, while Equation [16] represent uniaxial compaction. When applying the obtained Poisson's ratio into these equations, it resulted in an increased stiffness by 11 times after the core sample compacted uniaxial. The significant change in Young's modulus was caused by the change of the stress path, from uniaxial compression to uniaxial compaction. The assumption for these calculations was an isotropic and linear elastic material.

$$\frac{\Delta\sigma_z}{\Delta\varepsilon_z} = E \qquad\qquad [15]$$

$$\frac{\Delta\sigma_z}{\Delta\varepsilon_z} = E * \frac{(1-\vartheta)}{(1+\vartheta)(1-2\vartheta)} \qquad\qquad [16]$$

4.2.4 Creep rate

The axial displacement between the heating periods were investigated to check for temperature dependency. The temperature interval at 50˚C and 80˚C lasted almost 100 hours longer than the others. This increased the credibility of these creep rates, while the creep rates at the other temperature intervals did not exhibit a fully developed trend. The creep rate at room temperature was the highest, probably because of pore pressure equilibration due to the delayed effect from the applied axial stress. At 90˚C and 100 ˚C the core sample was expanding in the axial direction. This could be caused by an initial thermal expansion before pore pressure equilibration, the actual creep rate at these temperatures might be obtained after 100 hours. The creep rate at 50˚C and 80˚C was 0.0151 $mStr/hr$ and 0.0054 $mStr/hr$ respectively.
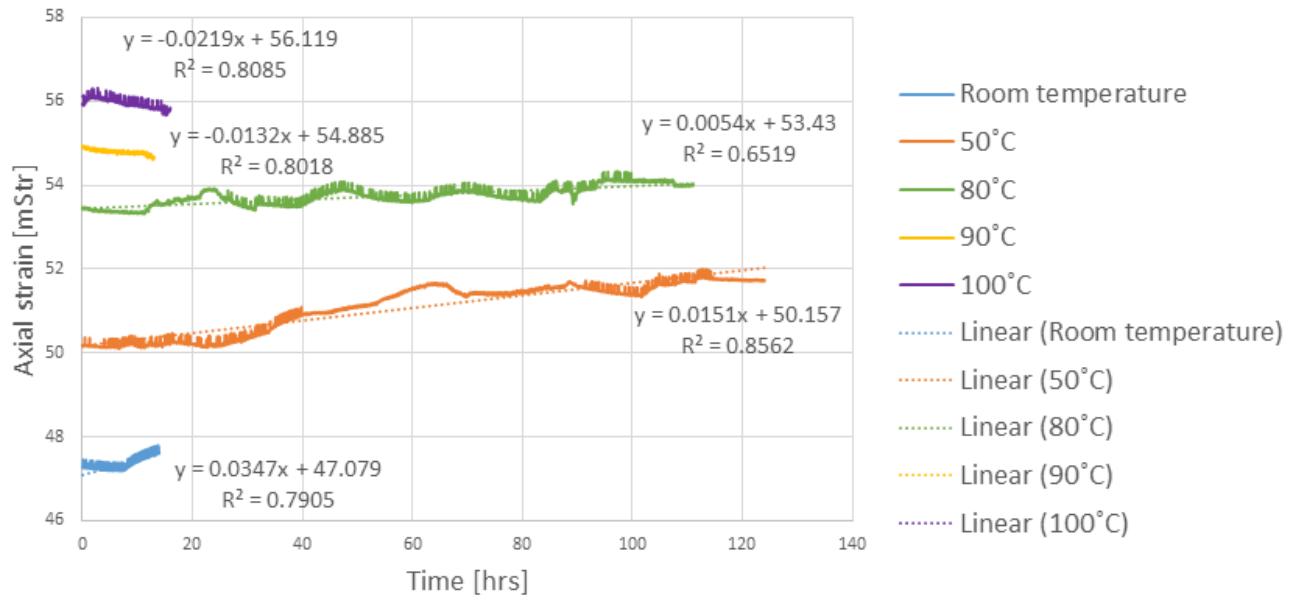
Figure 4.15: Axial strain of core sample 2 at different temperatures

4.2.5 Pump

The start of the second test consisted of increasing axial load and the pore pressure, this affected the cumulative volume as can be seen in Figure 4.16. An increase of the axial load caused a drop of the cumulative volume, while an increase of the pore pressure caused an increase of the cumulative volume.

48
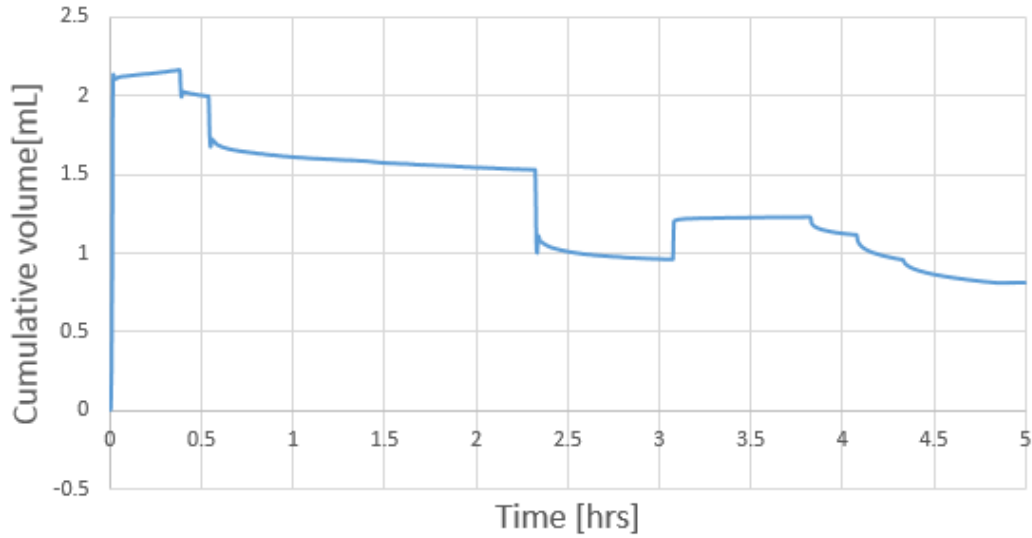
Figure 4.16: Cumulative volume provided by the pump during core sample 2

The pore pressure was set to $0.5\ MPa$ during the three first increases of the axial load, before it was set to $2\ MPa$ for the rest of the test as can be seen in Figure 4.17. The spikes was caused by the increased axial load.
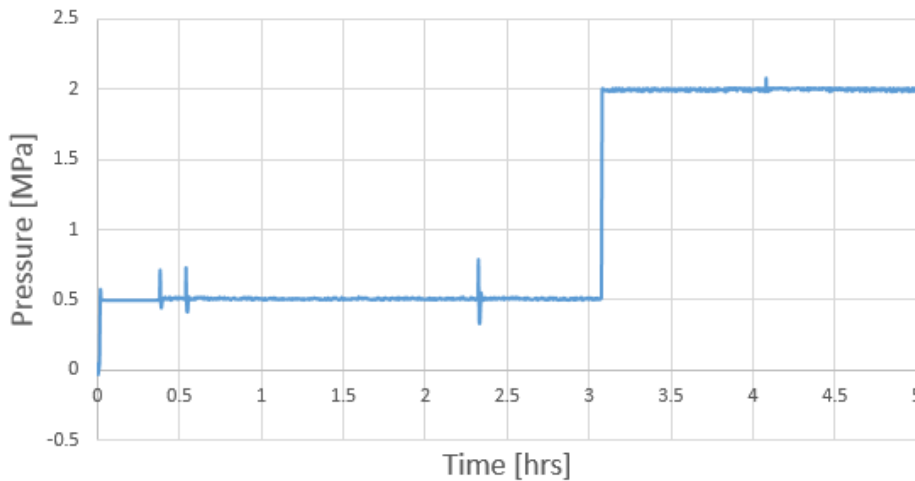
Figure 4.17: Pore pressure of core sample 2

The pore pressure controlled the pump rate, because the pump was set to maintain a constant pressure. For instance, when the pore pressure was set to $0.5\ MPa$ or $2\ MPa$ the pump had to deliver enough fluid to obtain these pressures as can be seen in Figure 4.18. The increased axial load affected the pump rate as well, spikes occurred when the axial load increased.
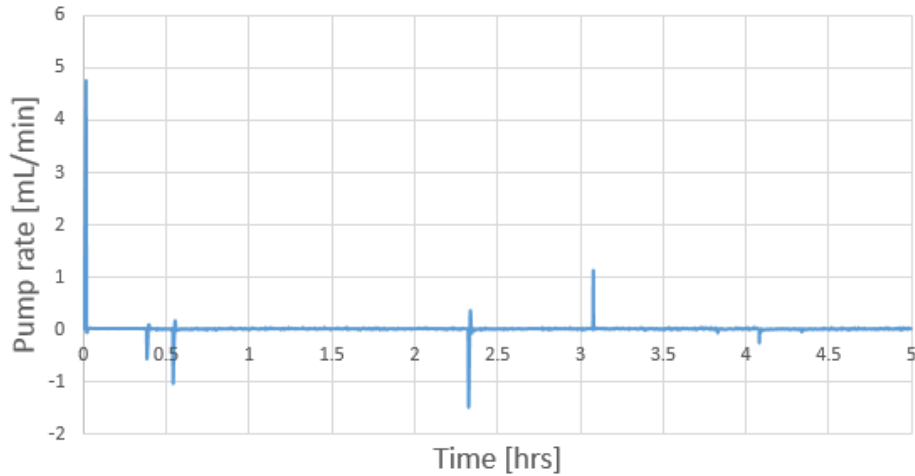
Figure 4.18: Pump rate of core sample 2

A constant cumulative volume, pore pressure and pump rate is a good indication of a closed system with no leakage.

4.2.6 Permeability Tests

Six permeability tests were taken in order to determine the permeability of the second core sample. The initial differential pressure of the permeability tests were more evenly distributed than the first core sample, all tests had an initial pressure below 4 bar. The two first permeability tests were conducted at room temperature, and the others were taken at 50 ˚C, 80 ˚C, 90 ˚C and 100 ˚C. Figure 4.19 depicts the permeability tests on a logarithmic scale, these tests lasted approximately 30 minutes until the differential pressure had equalized.
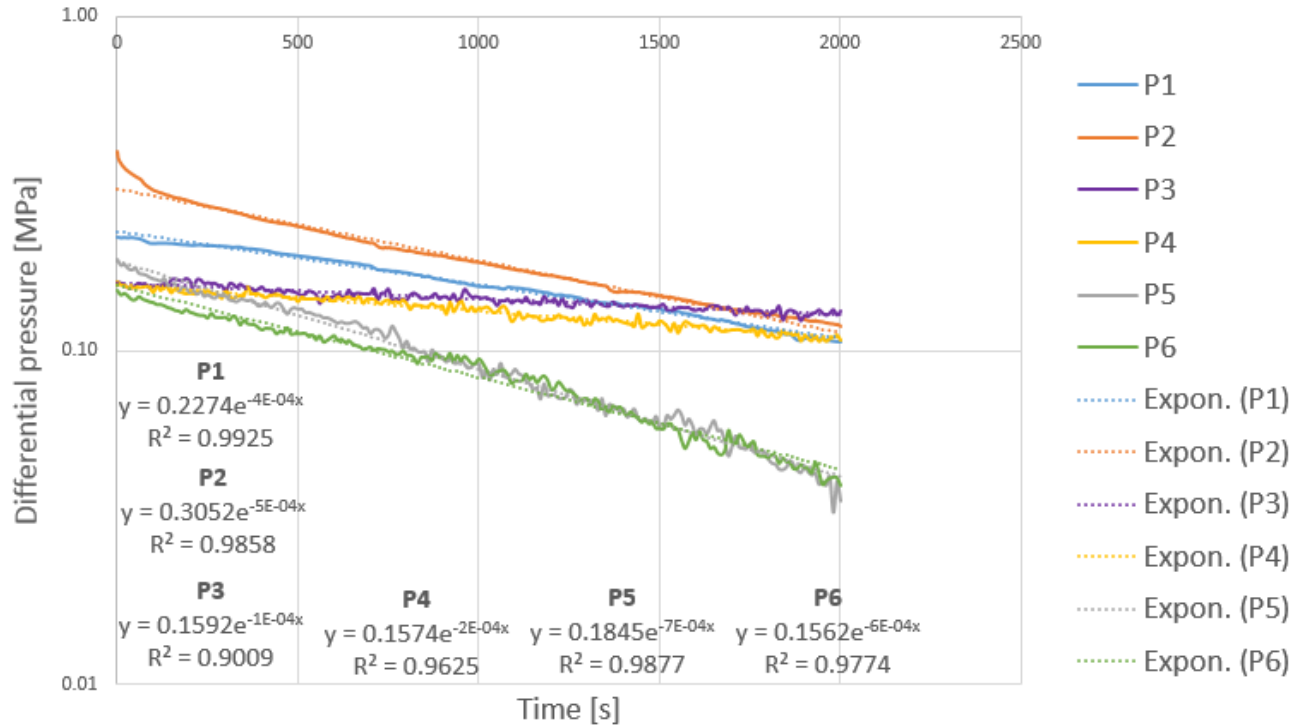
Figure 4.19: The permeability tests of core sample 2

The exponential trendlines fits the decline curves of the differential pressure since the R^2 values is close to 1. **Error! Reference source not found.** depicts the calculated permeability for the six permeability tests by using Equation [8]. Permeability test 3 and 4 had a slightly lower differential pressure decline than the other tests.

Permeability test [#]	Temperature [˚C]	Permeability [nD]
1	23	1672
2	23	2088
3	50	275
4	80	367
5	90	1140
6	100	875

Table 4.2: Permeability measurements of core sample 2

The axial strain was calculated when the permeability tests were conducted at the different temperatures, as depicted in Figure 4.20. The data points were obtained from Table 4.2. The axial strain increased as the core sample compacted in the axial direction.
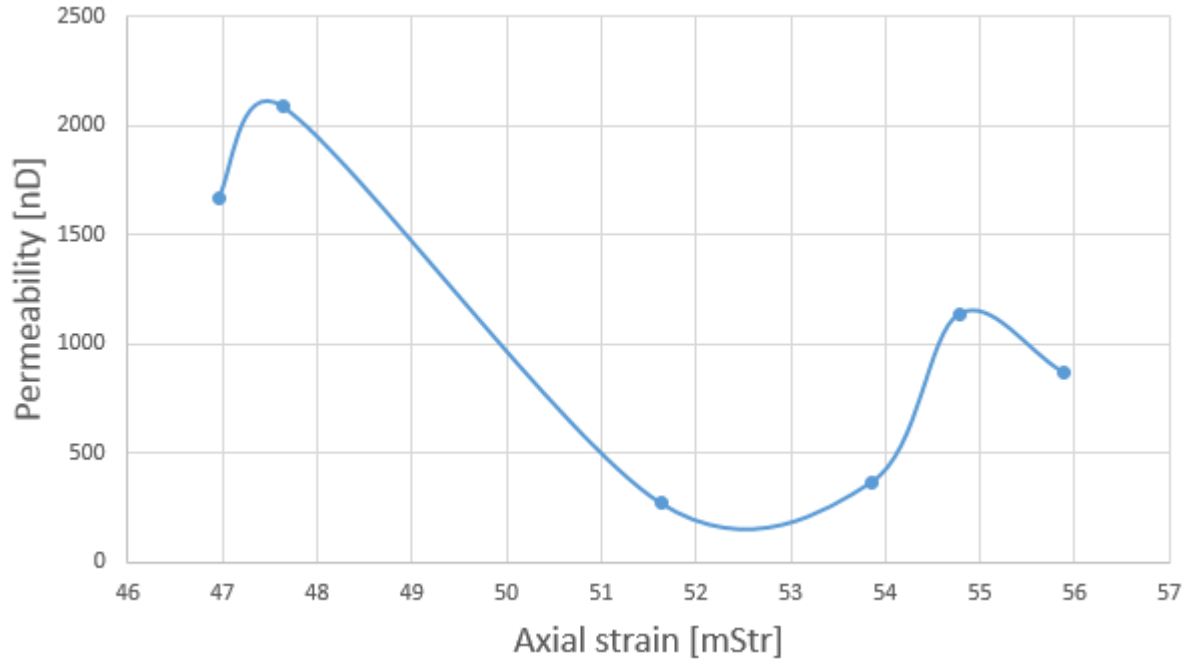
Figure 4.20: Axial strain plotted vs. permeability of the permeability tests of core sample 2

4.2.7 Strain Gauge Measurements

Figure 4.21 and Figure 4.22 depicts the corrected strain gauge measurements of channel 1 and channel 2 respectively. The strain gauge measurements from channel 1 fluctuated more and were approximately 3 MPa higher than the strain gauge measurements from channel 2. The reason for this is not known. The failure direction of the core sample might have caused a difference in the readings of the two channels, but not as much as 3 MPa.

Figure 4.21: Strain gauge measurements of channel 1 of core sample 2

The strain gauge measurements did not deviate significantly after the core sample had dilated onto the wall. The spikes were caused by the change in temperature.
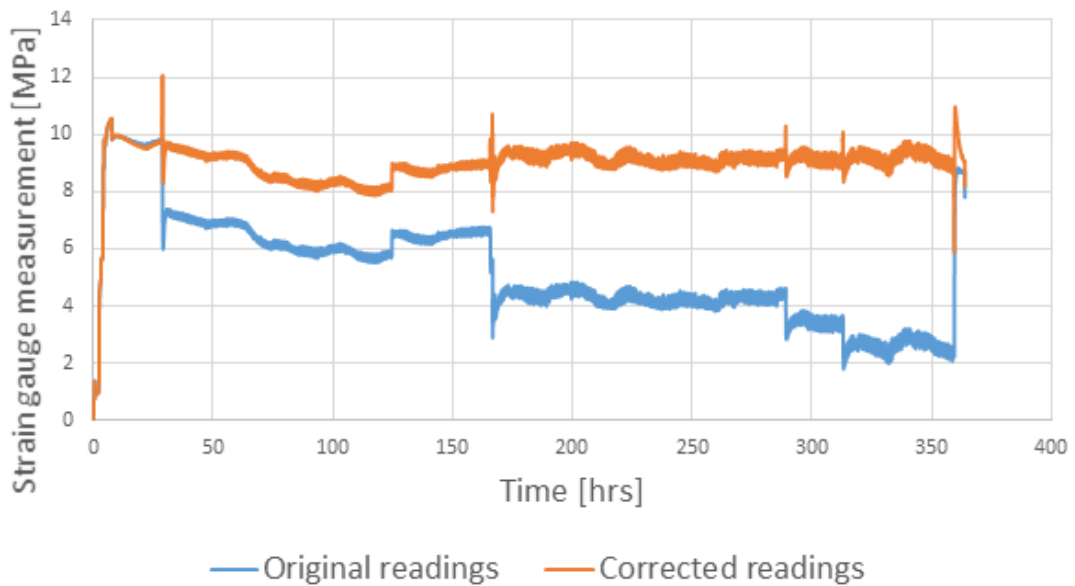
Figure 4.22: Strain gauge measurements of channel 2 of core sample 2

The core sample dilated onto the wall after approximately 2.5 hours due to a significant increase of the radial strain, as depicted in Figure 4.23. The contact occurred shortly after the axial load was increased to 15 kN. Consequently, the deformation behaviour changed from uniaxial compression to uniaxial compaction. The radial strain measurements increased further with increasing axial load.

53
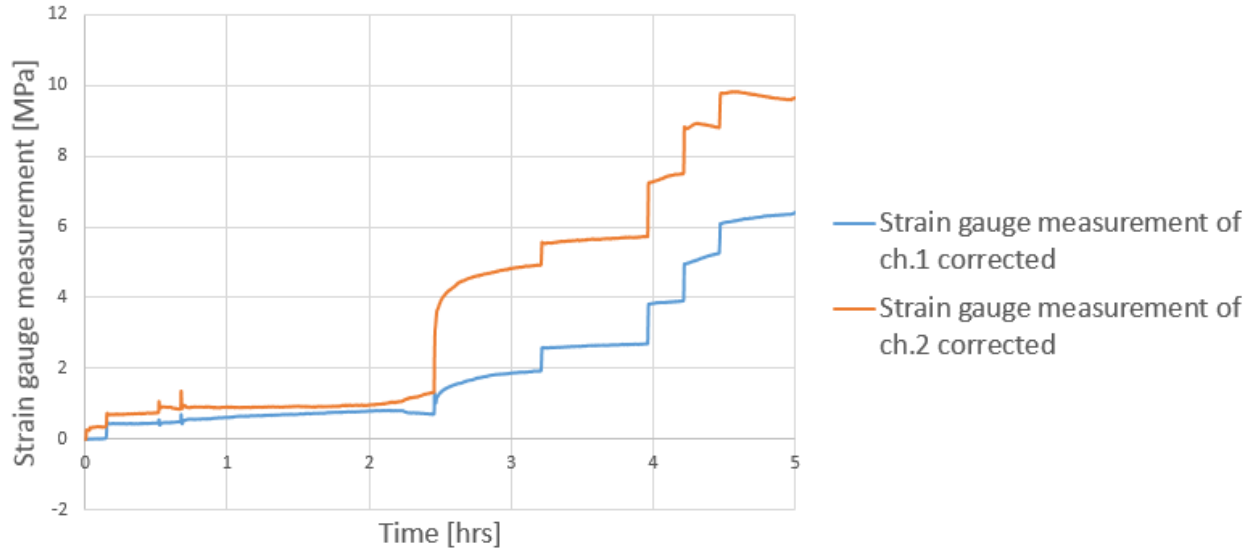
Figure 4.23: Radial strain measurement in start of the test of core sample 2

5 Discussion

Some companies have succeeded in using shale as an annular barrier in the North Sea in approximately 90 per cent of their tries, while other companies are failing. What could be the reason for this, and how can the success criterion be improved? Experiments were conducted on a Pierre shale to investigate creep behaviour, thermal effects and permeability.

There are many possible reasons why some companies succeeds in creating an argillaceous secondary annular barrier while other companies do not. Every shale formation is unique, and has to be treated differently based on its mineralogical composition, saturation, compaction history, pressure, temperature, geometry etc. The mineralogical composition and microfabric of the clay is especially important for the sealing properties, while the sealing process depends on the dilation of the clay. It is vital for the existence of the annular barrier that the surrounding stresses does not exceed the lowered failure strength of the dilated clay. An alternative to reduce the dilation distance is by expanding the casing towards the formation such as the formation do not have to expand as much, respectively increases the failure strength of the formation (Austbø, 2015).

5.1 Permeability Tests and Axial Strain

The permeability measurements of the first core sample were generally lower than the permeability measurements of the second core sample, especially at room temperature. The reason for a lower permeability at room temperature for the first core sample might be that it had compacted more when the permeability tests were conducted due to a larger temperature interval. The permeability of the tests at 50˚C and 80˚C were more alike, with the exception of the fourth test of the first core sample which resulted in a permeability of 33 nD. The permeability at 50˚C and 80˚C was approximately 250 nD and 333 nD respectively. The second core sample was heated further to 90˚C and 100˚C, where only one permeability test was taken at each step. These permeability values were in the range of 900 nD to 1100 nD, and were affected by a lower viscosity than the previous temperature steps. It should be noted that the permeability tests were not conducted at the same time for the two core samples, this affects the permeability calculation since Equation [8] contains several parameters that changes with time. It was the temperature dependency of the permeability which was of interest.

The axial strain values were similar in the first and second core sample, but the change in the axial strain was larger in the second core sample. Thus, the second core sample had a larger axial displacement than the first core sample, probably due to a higher temperature exposure.

5.2 Thermal Effects and Axial Displacement

The axial displacement measurements between the heating steps were of interest to determine the creep rate at the different temperatures. The first core sample was kept at room temperature for almost 12 days, this resulted in accurate measurements. The creep rate was rapid the first 100 hours, before it started to equalize. Based on this observation, all the temperature steps should have lasted for 100 hours to determine how the increased temperatures affected the axial displacement of the core samples. This was only carried out in two other temperature intervals, namely the 50˚C and the 80˚C temperature step in the second core sample due to time constraints. The other temperature steps in the second core sample lasted for approximately 15 hours, this limits the credibility of the temperature effect on the axial displacement since the trend was not fully developed.

The displacement of the second and third water layer could be a probable cause for the lowered permeability during 50˚C and the 80˚C. This trend was observed in both of the core samples, where the permeability measurements were higher before and after these temperature steps. The smectites in the compacting clay might have expelled water at these two temperature ranges. Another possible explanation for the permeability trend could be presence of cracks in the core sample. After the core samples were extracted from the oedometer cell, there were visible cracks. This might explain the initial permeability if cracks originated after the applied stress reached its maximum. These cracks might have self-sealed when the temperature approached 50˚C or 80˚C, which resulted in a lower permeability before the water dissipated at elevated temperatures and increased the permeability.

The last two temperature steps of the second core sample exhibited an axial thermal expansion, this was also observed in the tri-axial tests on the Pierre shale. However, an increase of the creep rate in the experiments was not observed with increasing temperatures as it was in the tri-axial tests. Loss of heated pore water might be the cause for the creep rate decrease.

5.3 Possible methods for Enhancing the Creep Rate

Figure 5.1 depicts some methods that might enhance the creep rate in a borehole. The temperature induced method is a thermal source that contributes to the dilation of the shale. The reason for using these methods is to increase the creep rate since it usually takes a long time for the clay to expand onto the casing, but by doing so it could also result in pore water loss and contraction of the formation which is counterproductive (Austbø, 2015).
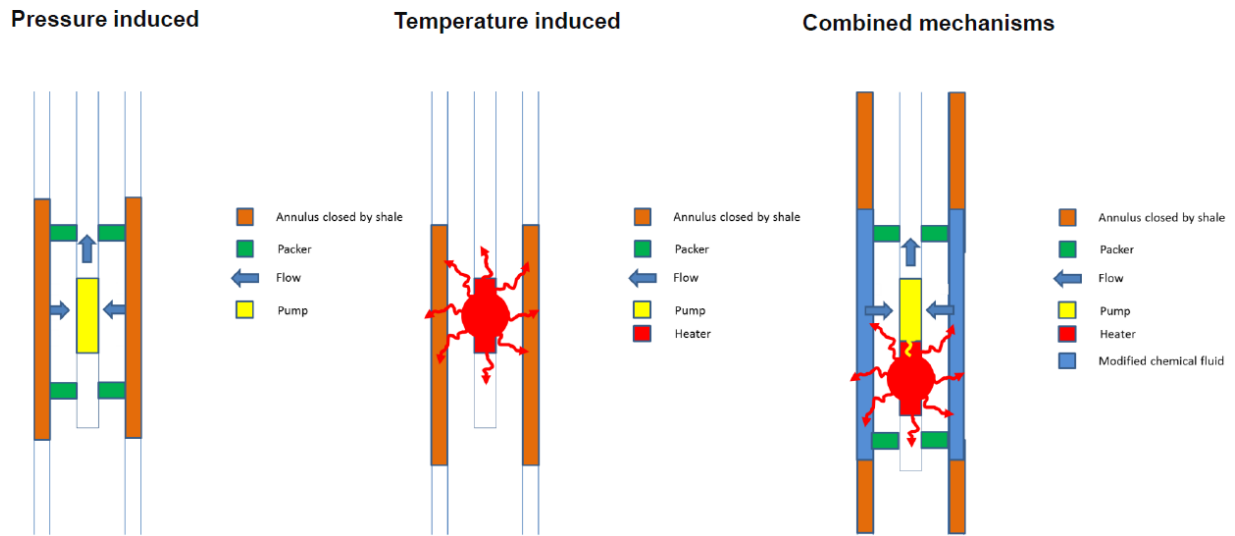
Figure 5.1: Possible methods for enhancing the creep rate (Kristiansen, 2015)

There are large cost savings related to creating a natural secondary annular barrier instead of an artificial one, but since the creep mechanism is not yet fully understood, further fundamental research is required to understand the limitations of this approach.

5.4 Further Work

More tests should be conducted on the Pierre shale to increase the credibility of the results. An interesting aspect is how rock failure affects the sealing properties of the shale. This can be tested by having two different annulus sizes. In the first test, the annulus should be made smaller than the expected "elastic" radial deformation so the gap is closing before the rock fails. In the second test, the annulus should be larger, so that rock failure happens before the sample touches the outer wall. The experiments could also use different annulus fluid, for instance with a different salt concentration. The second core sample was sent to another laboratory in order to make a µCT of it, but the results was not obtained due to time constraints. It should also be looked into whether an ultrasonic pulse echo measurement on the outer wall is feasible in order to detect the transition between fluid and shale filled annulus.

57

6 Conclusion

The use of an argillaceous rock as a secondary annular barrier is desirable given the proper sealing abilities. Using the formation as a sealing barrier instead of an artificial barrier have several advantages. There would be large cost savings since the cementation job for creating an annular barrier is not required, better integrity of the casing since the casing remains undamaged, and a better sealing efficiency due to the use of a natural barrier which provides a safer barrier than an artificial one. Shales have been investigated as natural barriers based on the sealing properties.

Two experiments on a Pierre shale have been conducted to determine the time dependent deformation, thermal effects and axial permeability. Based on the experimental results the following findings have been made;

- The third and second water layer might have an impact on the permeability due to the displacing water at approximately 50˚C and 80˚C.
- At temperatures higher than 80 ˚C the core samples expanded in the axial direction
- The stiffness of the second core sample increased significantly after the transition from uniaxial compaction to uniaxial compression.
- The second core sample had a larger axial displacement than the first core sample due to a higher temperature exposure.
- The creep rate at different temperatures did not deviate significantly during the tests, probably due to short temperature steps.

The obtained experimental results were only an indication of how creep and temperature affected the permeability and sealing properties of the testes Pierre shale. The results were not reliable because of experimental challenges. More tests and experiments are needed before any conclusions can be drawn.

Bibliography

Aglient-Technologies. (2002). *Laser and Optics User's Manual, chapter 17: Material Expansion Coefficients.*

Austbø, L. E. (2015). *Creep of Clay and Shale - Experience From Radioactive Waste Disposal Studies.*

Bauer, H. S. (2014). *Thermally Induced Compaction of Shales.*

Blümling, B. L. (2006). *The excavation damaged zone in clay formations time-dependent behaviour and influence on performance assessment.*

Cekerevac, L. (2003). *Experimental study of thermal effects on the mechanical behaviour of a clay.*

Chiarelli, L. S. (2000). *Influence of mineralogy and moisture content on plasticty and induced anisotropic damage of a claystone: application to nuclear waste disposal.*

Cimbala, Y. A. (2006). *Fluid Mechanics - Fundamentals and Applications.*

Colten-Bradley, V. (1987). *Role of Pressure in Smectite Dehydration - Effects on Geopressure and Smectite-to-Illite Transformation.*

Corkum. (2005). *Behaviour of Opalinus Clay around deep underground excavations.*

Cristescu, H. (1998). *Time Effects in Rock Mechanics.*

Daly, C. H. (2003). *Thick Walled Cylinders.*

Davy, S. B. (2006). *Permeability of macro-cracked argillite under confinement: Gas and water testing.*

Fabre, P. (2006). *Creep and time-dependent damage in argillaceous rocks.*

Fjær, H. H. (2008). *Petroleum Related Rock Mechanics 2nd edition.*

Fouche, W. L. (2004). *Fabric control on strain and rupture of hetereogeneous shale samples by using a non-conventional mechanical test.*

Horseman, H. H. (1996). *Water, gas and solute movement through argillaceous media.*

Klinkenberg, D. S. (2008). *Mont Terri Project: Comparison of Opalinus Clay and Callovo-Oxfordian clay-stone with respect to mechanical strength and carbonate microfabric.*

Kristiansen, G. A. (2015). Why Shale Could be Used as a Permanent Well Barrier Element. *Plug & Abandonment Seminar 2015* (p. 14). Stavanger: BP.

Li, W. (2013). *Effect of Thermally Induced Deformation of Shale on Wellbore and Caprock Integrity.*

Micro Measurements, V. P. (2015). *125UT - Datasheet, General Purpose Strain Gages—Tee Rosette.*

Nagra. (2002). *Projekt Opalinuston: Synthese der geowissenschaftlichen Untersuchungsergebnisse.*

Neuman, H. S. (2005). *Experimental investigations on anisotropy in dilatancy, failure and creep of Opalinus Clay.*

NORSOK, T. S. (n.d.). *Well Integrity in drilling and well operations, standard D-010.*

Peet, H. B. (2011). *Prediction of Thermal Conductivity of Steel.*

Pico-Technology. (2013). *USB TC-08 User's Guide.*

Schnier, S. (2006). *LT Experiment: Strength tests on cylindrical specimens, documentation and evaluation.*

Touloukian, S. H. (1975). *Thermophysical Properties of Matter.*

Ubilla, J. (2007). *LVDT Calibration Procedure.*

Wang, B. a. (1992). *Seismic Properties of Pore Fluids.*

Williams, C. C. (2009). *Identification and Qualification of Shale Annular Barriers Using Wireline Logs During Plug and Abandonment Operations*, 15.

Xu, Y. W. (2011). *Thermal Impact on Shale/Failure Behaviours - Laboratory Studies.*

Zhang, R. S. (2006). *Experimental study of the thermo-hydro-mechanical-behavoiur of indurated clays.*

Appendix

Applied Force and Stress Acting on the Core Samples

Number	Weights [kg]	Force [N]	Stress [Pa]
1	25.82	2532.9	2.26E+06
2	25.75	2526.1	2.26E+06
3	25.76	2527.1	2.26E+06
4	25.86	2536.9	2.27E+06
5	25.84	2534.9	2.27E+06
6	25.76	2527.1	2.26E+06
7	25.7	2521.2	2.25E+06
8	25.82	2532.9	2.26E+06
9	25.91	2541.8	2.27E+06
10	25.85	2535.9	2.27E+06
11	9.86	967.3	8.65E+05
12	9.86	967.3	8.65E+05
13	9.82	963.3	8.61E+05
14	9.94	975.1	8.72E+05
TOT	**297.55**	**29189.66**	**2.61E+07**

Strain gauges specifications

Grid resistance [Ω]	120 ±0.4%
Temperature range [˚C]	-75 to 175
Strain range	±5%
Gauge factor, grid #1	2.090±0.5%
Gauge factor, grid #2	2.115±0.5%

Fluid Dynamic Viscosity

Temperature [°C]	Water viscosity [cP]	Brine viscosity [cP]
20	1.002	1.074
25	0.890	0.977
30	0.797	0.893
35	0.718	0.820
40	0.651	0.755
45	0.594	0.698
50	0.544	0.647
55	0.501	0.601
60	0.463	0.560
65	0.430	0.523
70	0.400	0.489
75	0.374	0.459
80	0.351	0.432
85	0.330	0.406
90	0.311	0.384
95	0.294	0.363
100	0.279	0.344

Water: $\mu = a10^{(b/(T-c))}$, $\quad a = 2.414 * 10^{-5}\ N * s/m^2$, $\quad b = 247.8\ K$, $\quad c = 140K$

Brine: $\mu = 0.1 + 0.333S + (1.65 + 91.9S^3)exp\{-[0.42(S^{0.8} - 0.17)^2 + 0.045]T^{0.8}\}$, S=0.035

Accurate Measurements of the Core Samples

	Core sample 1	Core sample 2
d1 [mm]	37.770	37.720
d2 [mm]	37.750	37.760
d3 [mm]	37.770	37.720
d4 [mm]	37.760	37.740
d_avg [mm]	37.763	37.735
h1 [mm]	41.220	41.250
h2 [mm]	41.260	41.100
h3 [mm]	41.240	41.200
h_avg [mm]	41.240	41.183
Mass [g]	110.1	109.9

IV

Fluid Density

Water: $\Delta\rho_w = -\beta\rho_{w,1}\Delta T$, $\qquad \rho_{w,2} = \rho_{w,1} + \Delta\rho_w$

Temperature [˚C]	ΔT_avg [˚C]	β [1/K]	Average β [1/K]	Δρ [kg/m^3]	Water density from table [kg/m^3]	Water density from Equation [kg/m^3]
20	20	0.000195	0.000195	0.00	998	998.00
25	22.5	0.000247	0.000221	-1.10	997	996.90
30	25	0.000294	0.000247	-2.47	996	995.53
35	27.5	0.000337	0.0002705	-4.05	994	993.95
40	30	0.000377	0.000294	-5.87	992.1	992.13
45	32.5	0.000415	0.0003155	-7.87	990.1	990.13
50	35	0.000451	0.000337	-10.09	988.1	987.91
55	37.5	0.000484	0.000357	-12.47	985.2	985.53
60	40	0.000517	0.000377	-15.05	983.3	982.95
65	42.5	0.000548	0.000396	-17.78	980.4	980.22
70	45	0.000578	0.000415	-20.71	977.5	977.29
75	47.5	0.000607	0.000433	-23.77	974.7	974.23
80	50	0.000653	0.000451	-27.01	971.8	970.99
85	52.5	0.00067	0.0004675	-30.33	968.1	967.67
90	55	0.000702	0.000484	-33.81	965.3	964.19
95	57.5	0.000716	0.0005005	-37.46	961.5	960.54
100	60	0.00075	0.000517	-41.28	957.9	956.72

Brine: $\rho_{brine} = \rho_w + S\{0.668 + 0.44S + 10^{-6}[T(80 + 3T - 3300S)]\}$, $\quad$ S=0.035

Temperature [˚C]	Water density [kg/m^3]	Water density [g/cm^3]	Brine density [g/cm^3]	Brine density [kg/m^3]
20	998	0.998	1.022	1021.9
25	997	0.997	1.021	1021.0
30	996	0.996	1.020	1020.0
35	994	0.994	1.018	1018.0
40	992.1	0.9921	1.016	1016.1
45	990.1	0.9901	1.014	1014.2
50	988.1	0.9881	1.012	1012.2
55	985.2	0.9852	1.009	1009.4
60	983.3	0.9833	1.008	1007.5
65	980.4	0.9804	1.005	1004.7
70	977.5	0.9775	1.002	1001.8
75	974.7	0.9747	0.999	999.1
80	971.8	0.9718	0.996	996.3
85	968.1	0.9681	0.993	992.7
90	965.3	0.9653	0.990	990.0
95	961.5	0.9615	0.986	986.2
100	957.9	0.9579	0.983	982.7

Poisson's Ratio and Young's Modulus

$$\frac{\Delta\sigma_r}{\Delta\sigma_z} = \frac{\vartheta}{(1-\vartheta)} \qquad\qquad \frac{\Delta\sigma_z}{\Delta\varepsilon_z} = E \qquad\qquad \varepsilon_z = \frac{\Delta L}{L}$$

$$\varepsilon_r = \frac{\Delta R}{R} \qquad\qquad \frac{\Delta\sigma_z}{\Delta\varepsilon_z} = E * \frac{(1-\vartheta)}{(1+\vartheta)(1-2\vartheta)} \qquad\qquad \frac{\varepsilon_r}{\varepsilon_z} = -\vartheta$$

Approximately when core sample touches the wall (before). Uniaxial compression

Axial strain	0.0315 [mm/mm]				
Radial strain	0.0150 [mm/mm]				
v (Poisson)	0.476				

After it touched the wall (values are found from the graph)

Δσ_r	5.84 MPa			6.9	1.062
Δσ_z	6.21 MPa			8.42	2.21
v (Poisson)	0.485				

Petrophysical Properties of the Core Samples

Mineral	%
Quartz	16.0
K-fsp.	0.0
Plag.	8.55
Chl.	29.6
Kaol.	0.0
Illite	19.9
ML	0.0
Smect.	19.8
Calc.	1.54
Sid.	1.43
Dol/Ank	2.63
Pyr	0.63

Porosity: 20.8%

VI

Calibration

Time [min]	Time [hrs]	Temp [˚C]	Ch.1 [bar]	Ch.2 [bar]
End of temp. Interval 1 (30˚C)				
225	3.75	30.32	29.17	36.83
226	3.77	30.31	29.84	36.77
227	3.78	30.32	29.03	36.71
228	3.80	30.34	30.55	36.93
229	3.82	30.34	30.02	37.06
		30.33	**29.72**	**36.86**
End of temp. Interval 2 (65˚C)				
370	6.17	67.1	-13.40	-2.05
371	6.18	67.1	-12.26	-1.92
372	6.20	67.11	-13.41	-2.33
373	6.22	67.1	-13.98	-2.08
374	6.23	67.1	-13.55	-1.28
		67.10	**-13.32**	**-1.93**
End of temp. Interval 3 (100˚C)				
453	7.55	104.05	-50.15	-39.29
454	7.57	104.02	-51.20	-38.00
455	7.58	104.03	-50.20	-37.75
456	7.60	104.05	-50.74	-38.03
457	7.62	104.04	-51.20	-38.10
		104.04	**-50.70**	**-38.24**
End of temp. Interval 4 (65˚C)				
1370	22.83	67.13	-14.15	-3.28
1371	22.85	67.13	-12.60	-2.82
1372	22.87	67.11	-14.74	-2.97
1373	22.88	67.11	-14.49	-2.74
1374	22.90	67.11	-14.47	-3.08
		67.12	**-14.09**	**-2.98**
End of temp. Interval 5 (30˚C)				
1612	26.87	30.4	18.14	25.31
1613	26.88	30.41	17.65	25.27
1614	26.90	30.42	17.70	25.20
1615	26.92	30.39	18.26	25.48
1616	26.93	30.4	17.87	25.22
		30.40	**17.93**	**25.29**

Ch.1 correction

Strain gauge measurement [bar] vs Temperature [°C]

$y = -0.9321x + 47.558$
$R^2 = 0.9971$

Ch.2 correction

Strain gauge measurement [bar] vs Temperature [°C]

$y = -0.863x + 53.498$
$R^2 = 0.9922$
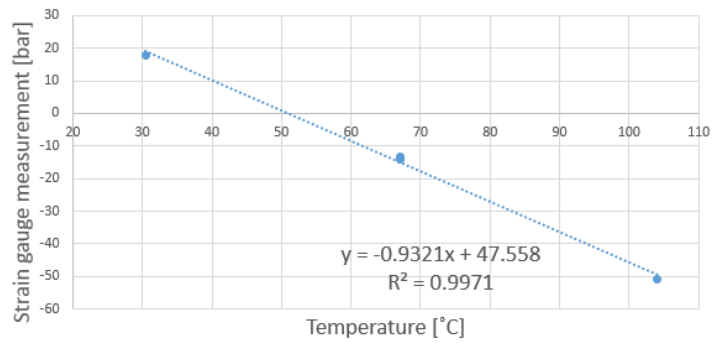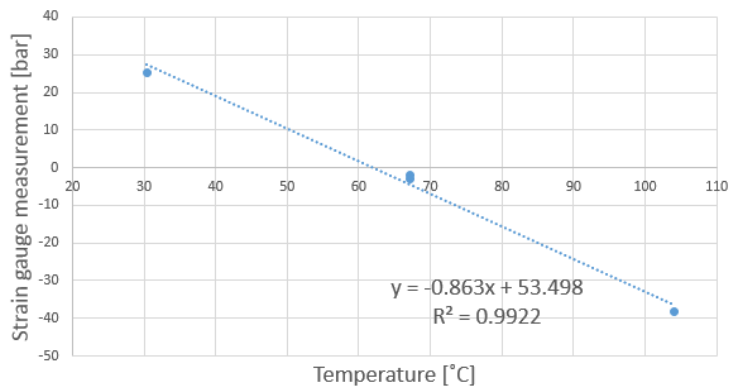
Permeability

Test ID	Time [s]	Thickness (height) [mm]	Diameter [mm]	Area [m2]	Temperature [C]	Axial stress [MPa]	Pore pressure [MPa]	Axial strain [mm/m]	Dynamisk viskositet [Pa*s]	Km [Pa/m3]	Alpha [1/s]	Permeability [m2]	Permeability [nD]
P1	277576	35.62	37.763	0.0011	25	8.1	2	49.27	0.000977	4.16E+12	0.00010	3.73E-19	378
								49.27					378
P2	882703	35.61	37.763	0.0011	50	8.1	2	49.53	0.000647	4.16E+12	0.00010	2.47E-19	250
P3	1029300	35.61	37.763	0.0011	50	8.1	2	49.51	0.000647	4.16E+12	0.00007	1.73E-19	175
P4	1168460	35.54	37.763	0.0011	80	8.6	2	51.38	0.000432	4.16E+12	0.00002	3.29E-20	33
P5	1264074	35.49	37.763	0.0011	80	8.9	2	52.82	0.000432	4.16E+12	0.0002	3.29E-19	333

Test ID	Time [s]	Thickness (height) [mm]	Diameter [mm]	Area [m2]	Temperature [C]	Axial stress [MPa]	Pore pressure [MPa]	Axial strain [mm/m]	Dynamisk viskositet [Pa*s]	Km [Pa/m3]	Alpha [1/s]	Permeability [m2]	Permeability [nD]
P1	29770	39.25	37.7	0.0011	25	8.4	2	46.96	0.000977	4.16E+12	0.0004	1.65E-18	1672
P2	104134	39.22	37.7	0.0011	25	8.4	2	47.64	0.000977	4.16E+12	0.0005	2.06E-18	2088
P3	531722	39.06	37.7	0.0011	50	8.5	2	51.63	0.000647	4.16E+12	0.0001	2.72E-19	275
P4	947592	38.97	37.7	0.0011	80	8.7	2	53.85	0.000432	4.16E+12	0.0002	3.62E-19	367
P5	1123864	38.93	37.7	0.0011	90	8.7	2	54.79	0.000384	4.16E+12	0.0007	1.13E-18	1140
P6	1293784	38.88	37.7	0.0011	100	8.8	2	55.88	0.000344	4.16E+12	0.0006	8.63E-19	875

VIII

Transducer Connection

9 Transducer connection

9.1 Full bridge, SG

Supported by the following modules: MX840/A, MX440A, MX410/B, MX1615/B

MX1615/B
Push in

Loading cell ↓   Strain gauge ↓

				MX1615/B
wh	Measurement signal (+)	Brun	5	Start 6
bk	Excitation (-)	Grønn	2	Grønn 4
b u r d	Excitation (+)	Gul	3	Rød 2
ye	Measurement signal (-)	Kvit	10	Kvit 7
gn	Cable shield		Hsg.	8
gy	Sense lead (+)		8	3
	Sense lead (-)		7	5

Jomper, enleder → (rød)

4
9
6
1   1

1 ⊥
2 Data
3 No function

1-wire EEPROM (optional)
view from below

1 2 3

Hsg. = Housing

Cable color code: wh= white; bk= black; bu= blue; rd= red; ye = yellow; gn= green; gy= gray

IX